Title: Modulating radical propagation in proteins by proton-coupled electron transfer and hydrogen bonding

Rebecca K. Zawistowski[1,2], *Timothée Chauviré*[1,2], *Sutanuka Mana*[1],

Nandini Ananth[1] *and Brian R. Crane*[1,2*]

[1]Department of Chemistry and Chemical Biology,

[2]Weill Institute for Cell and Molecular Biology, Cornell University

Ithaca, NY 14853, USA

Abstract

Long-range protein electron transfer (ET) often depends on tryptophan and tyrosine residues acting as radical relay sites. For example, cytochrome c peroxidase (CcP) generates a $W191^{\bullet+}$ radical to increase ET from cytochrome c (Cc) to the active center. W191 substitution to Tyr reduces ET rates, but introduction of an adjacent general base at position 232 (as Glu or His) recovers activity. E232 fluorination shifts the ET pH dependence to lower values, verifying that a hydrogen bond elevates the $Y191^{\bullet}$ formal potential for effective ET. Photoinitiated ET between Zn-porphyrin (ZnP) CcP (ZnCcP) and Cc also depends on activating Y191 with a basic residue, but through a different mechanism than for the peroxide-driven system. In ZnCcP, pH dependencies and solvent isotope effects indicate that proton-coupled electron transfer to the basic residue and $ZnP^{\bullet+}$, respectively, facilitate $Y191^{\bullet}$ formation. Replacing Cc with the irreversible oxidant $[Co(NH3)_5Cl]^{2+}$ isolates distinct protein radicals for characterization by Electron Paramagnetic Resonance (EPR) spectroscopy. Radical distributions reveal that $W191^{\bullet+}$ lies ~15 mV in potential below $ZnP^{\bullet+}$ and that the two radicals exchange on a slow time scale despite their close separation. Remarkably, ZnCcP Y,G191:E,H232 variants propagate radicals differently to peripheral sites depending on the nature of the 232 residue. QM/MM calculations support radical exchange between $ZnP^{\bullet+}/Trp^{\bullet+}$ and the importance of a hydrogen bond to $Y191^{\bullet}$ for maintaining a high potential to oxidize peripheral donors. These resolved reactivity patterns of CcP/ZnCcP have general relevance for engineering proton management to separate and migrate charge in proteins and potentially other molecular systems.

Introduction

Protein long-range electron transfer (ET) is a centrally important process to many metabolic

pathways including cellular respiration and photosynthesis [1–3]. Electrons transfer through

protein matrices via the oxidation and reduction of redox active cofactors separated by >10 Å or

more. Despite these long distances, long-range ET reactions can occur at remarkably fast rates,

exceptional specificity, and with little loss in free energy [1–3]. Over very long distances, redox active protein residues, primarily tryptophan and tyrosine, facilitate multi-step ET by acting as

Scheme 1. Reaction mechanism for Fe(III) CcP and Fe(II) Cc with H_2O_2

$$\text{Fe(III) CcP} + H_2O_2 \rightarrow \text{Fe(IV)=O CcP (W191}^{\bullet+}\text{)} + H_2O \quad (1)$$

$$\text{Fe(IV)=O CcP (W191}^{\bullet+}\text{)} + \text{Fe(II) Cc} \rightarrow \text{Fe(IV)=O CcP (W191}^{0}\text{)} + \text{Fe(III) Cc} \quad (2)$$

$$\text{Fe(IV)=O CcP (W191}^{0}\text{)} + H^+ \rightleftharpoons \text{Fe(III)-OH CcP (W191}^{\bullet+}\text{)} \quad (3)$$

$$\text{Fe(III)-OH CcP (W191}^{\bullet+}\text{)} + \text{Fe(II) Cc} + H^+ \rightarrow \text{Fe(III) CcP (W191}^{0}\text{)} + \text{Fe(III) Cc} + H_2O \quad (4)$$

oxidizable hole-hopping relay sites [4,5]. For example, Trp and Tyr radical intermediates migrate charge over distances that can span over 30 Å in systems such as ribonucleotide reductases (RNR), cryptochromes, BLUF photoreceptors, peroxidases, and photosystem II (PSII) [6–9]. Despite the ability of high potential metallocenters or photoexcited cofactors to oxidize either Trp or Tyr, these residues are often not interchangeable owing to their different sensitivities to local environment and the different pK_as of their radical cations. Indeed, Proton-Coupled ET (PCET) plays a critical, complex and still understudied role in hole-hopping through Trp and Tyr. For example, in PSII, PCET reactions of TyrZ and a nearby His residue allow $P680^+$ to efficiently transfer electron holes to the oxygen evolving complex for water splitting [10-12]. Furthermore, multistep ET reactions involving Trp/Tyr also have the potential to generate spin-correlated radical pairs (SCRPs) with relatively long phase-memory times [13]. Such SCRPs have the potential to be exquisitely sensitive detectors of local environment and have been implicated in, for example, the avian magnetic compass [14]. However, Trp and Tyr radicals have high redox potentials and proteins provide many reactive sites. Thus, controlling reactivity is non-trivial. Investigating how local environment modulates relay residue redox chemistry will help us better understand mechanisms that underlie fundamental biological sensing and energy conversion.

The complex formed between yeast cytochrome c peroxidase (CcP) and cytochrome c (Cc) has long stood as a model system for understanding long-range interprotein ET [15–19]. Moreover, it contains one of the most thoroughly characterized Trp radicals, which has been analyzed in detail by EPR spectroscopy [18,20–22]. CcP reacts with H_2O_2 to form Compound I (Cpd 1), which contains the ferryl heme and a second oxidized equivalent on W191 (**Scheme 1**). Fe(IV)=O CcP is then reduced sequentially by two equivalents of Fe(II) Cc. $W191^{\bullet+}$ in Cpd I oxidizes the Fe(II) Cc heme which is 22 Å away (**Figure 1a**). Substitution of W191 to Gly or Phe (G/F191 CcP) eliminates CcP activity. Surprisingly, switching W191 for another oxidizable residue, Tyr (Y191 CcP) also renders CcP inactive, despite Y191 also forming a Cpd I-like state with peroxide [23]. Nonetheless, the activity of Y191 CcP can be partially rescued by introduction of an adjacent conjugate base (Y191:E/H232 CcP) [24]. His and Glu residues are

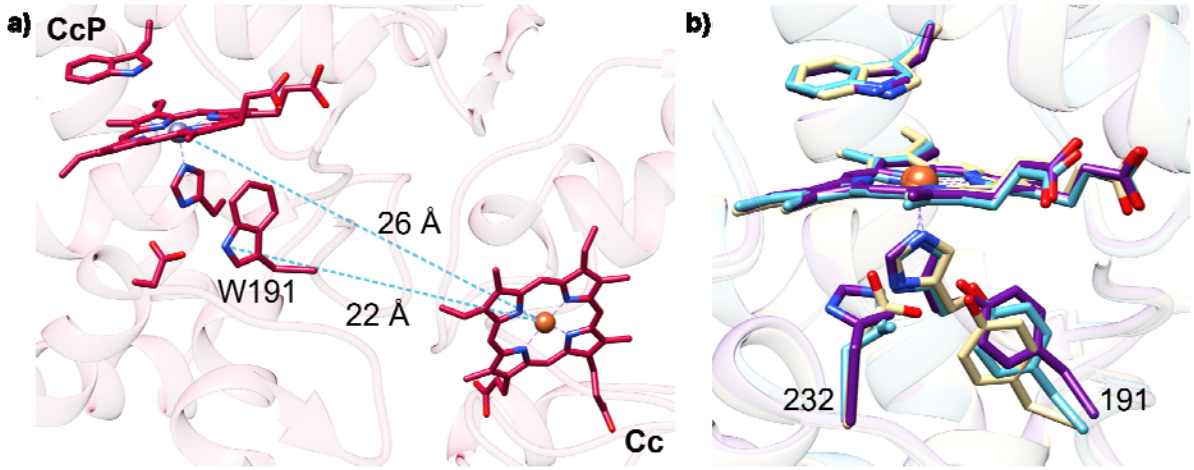

Figure 1. a) Distances between redox centers in the crystallographic CcP:Cc complex. **b)** Structural superpositions depict the Y191 environment in Y191 (blue), Y191:E232 (yellow), and Y191:H232 (purple) CcP in complex with Cc. (PDB codes: 1u74, 5cih, 6p41, and 6p42).

both able to accept a proton from Tyr upon oxidation and facilitate hydrogen bonding to the formed radical [10-12, 25]. Crystal structures of the Y191, Y191:E232 and Y191:H232 variants

reveal that the E/H232 residues are in close proximity of the Y191 hydroxyl group (**Figure 1b**). Spectroscopic and reactivity data suggest that the conjugate base maintains a E/H232-H^+-Y191$^\bullet$

Scheme 2. Photoinduced reaction scheme for ZnCcP

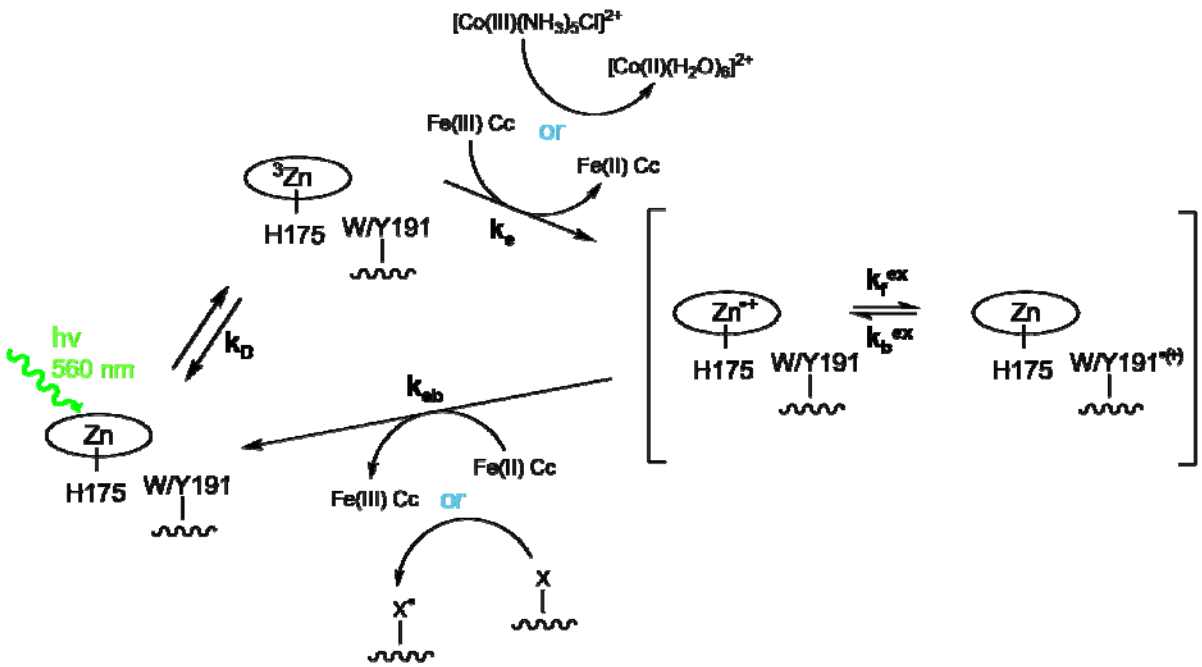

triad to elevate the formal potential of the relay site so that it can effectively oxidize Fe(II) Cc. In both the Y191:E232 and Y191:E232 variants, pH dependencies indicate that proton loss from the E/H232-H^+-Y191$^\bullet$, reduces the formal potential of the relay site, diminishing its ability to accept an electron from Fe(II) Cc.

Substitution of the CcP heme with zinc porphyrin (ZnCcP) allows light-activation of redox reactions with Cc [15,23,26–29] and thereby provides a useful system for further studying how the 191 relay site environment tunes ET (**Scheme 2**). For ZnCcP, 560 nm light excites zinc-porphyrin (ZnP) in CcP to the singlet state (^{1}ZnP), which then rapidly decays to a long-lived triplet state (^{3}ZnP), and in the absence of Fe(III) Cc relaxes back to the ground state with a rate

constant, k_D ~100 s^{-1} [28–31]. In the presence of Fe(III) Cc, ^{3}ZnP ejects an electron across the protein interface and reduces Cc, generating a charge separated species between $ZnP^{\bullet+}$ and Fe(II) Cc. Reduced Cc will then transfer an electron to CcP via hole-hopping through $W191^{\bullet+}$ with a similar ET mechanism as the native heme-peroxide system. The ability of a relay residue to accelerate net charge flux through a protein in part depends on the relay site formal potential relative to the donor and acceptor sites. In ZnCcP, a lower $W191^{\bullet+}$ potential relative to $ZnP^{\bullet+}$ localizes the hole closer to the donor, Cc, but also reduces the driving force to oxidize Cc. These factors play against each other in determining the net ET rate. The ZnCcP:Cc charge recombination reaction has been considered as a rapid hole exchange between $ZnP^{\bullet+}$ and $W191^{\bullet+}$ with the equilibrium lying toward $ZnP^{\bullet+}$ [32–34] i.e.

$$k_{obs} = K_{eq} k_{eb,}$$

$$K_{eq} = {[W191^{\bullet+}]}/{[ZnP^{\bullet+}]}$$

$K_{eq} \ll 1$, and k_{eb} being the rate constant for the single step ET reaction (**Scheme 2**):

$$ZnP\ W191^{\bullet+}\ Fe(II)Cc \rightarrow ZnP\ W191\ Fe(III)Cc$$

However, there has not been a direct experimental measurement of K_{eq}, a value that is challenging to assess given the high reactivity of the participating redox sites and low kinetic occupancy of the radical.

In efforts to leverage the well-studied CcP:Cc system to better understand the factors that allow relay sites to modulate protein ET, we have manipulated the pK_a of the conjugate base by incorporating a fluorinated derivative of the E232 and utilized a sacrificial electron acceptor that allows stable generation of radical states after ZnCcP photoexcitation. Together the results underscore the importance of proton transfer at the relay site for both the peroxide-driven natural

reaction of heme-containing CcP (FeCcP) and the photochemistry of ZnCcP. In the latter case, the nature of the base partner determines the ability of the radical to propagate elsewhere in the protein. These results provide insight into how perturbing hydrogen bonding and nearby proton donors or acceptors can inhibit or promote ET through relay sites and thereby offer insight into the design of effective longe range ET systems.

Results

Cc oxidation assays of globally incorporated F-Glu FeCcP

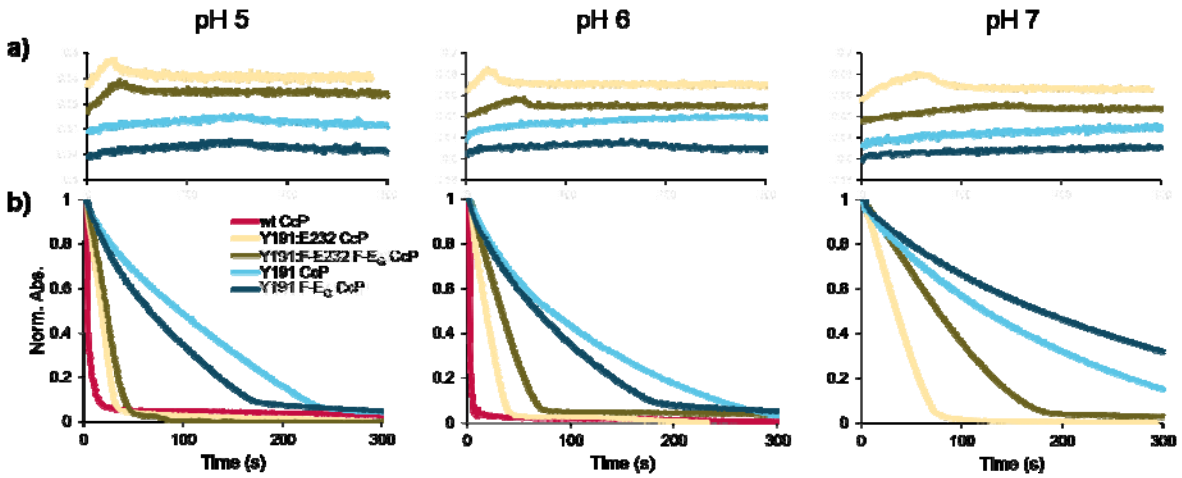

Figure 2. Cc oxidation rates of Y191 CcP variants under multiple turnover conditions (1 μM CcP, 30 μM Cc, 10 μM H_2O_2 in 100 mM KP_i buffer). **a)** Time traces for Fe(IV)=O formation and decay monitored at 434 nm. Globally incorporated F-Glu CcP variants were monitored in comparison to unsubstituted counterparts in varying pH buffers. At higher pH, the ferryl CcP species in Y191:F-E232 F-E_G is longer lived than in Y191:E232 CcP, similar to that of Y191 CcP. **b)** Time traces of Cc oxidation via CcP monitored at 550 – 540 nm. Both Y191:E232 and Y191:F-E232 F-E_G exhibit pH dependencies in the rate of Cc oxidation.

Previous work suggested that a hydrogen bond provided by the neutral acid form of E232 to Y191 increased the reduction potential of the tyrosyl radical to a range where it could effectively oxidize Cc [24]. To validate this mechanism, we sought to minimally perturb the E/H232-H^+-Y191$^\bullet$ triad by lowering the pK_a of the H-bonding residue such that it would become unprotonated at the pHs where ET activation was observed otherwise. The noncanonical amino acid 4-fluoro-glutamic acid (F-Glu) is predicted to have pK_a around 2 pH values lower than glutamic acid and will therefore be deprotonated at pH 5-8. F-Glu was globally incorporated into CcP using the endogenous translation machinery of an *E. coli* Glu auxotroph: PA-340 (*E. coli* Genetic Resource Center). The endogenous translation system should not differentiate between Glu or F-Glu due to their high structural similarity. Hence, supplementation with F-Glu upon

induction of CcP protein expression should result in at least partial F-Glu incorporation into CcP. To maximize F-Glu incorporation into CcP and limit toxicity associated with global incorporation, cells were initially grown to sufficient density in rich (Luria Broth) media, washed extensively with buffer and moved to a minimal media containing F-Glu, where expression was induced at 17 $^{\circ}$C. Mass spectrometry (MS) data were collected of the purified F-Glu containing apo-CcP (**Figure S1**). Extracted ion chromatograms (XICs) indicated that ~50 % of the ionized CcP tryptic peptide containing position 232 had F-Glu instead of Glu (**Table S2**). This is likely a lower bound on the incorporation level because F-Glu containing peptides are known to ionize less under ESI-MS positive mode than their Glu analogs [35].

In this approach, CcP can undergo global (F-E_G) F-Glu substitution in any of its 20 endogenous Glu residues. Given the potentially complicating effects of global incorporation coupled with incomplete incorporation at the 232 site, we made reactivity comparisons among four variants: Y191, Y191 F-$E_{G,}$ Y191:E232, and Y191:F-E232 F-$E_{G.}$ Rates of CcP Cpd I reduction by Fe(II) Cc were measured over multiple turnovers (**Scheme 1**) by monitoring Fe(II) Cc oxidation (550 – 540 nm) and progress of the ferryl Fe(IV)=O CcP (434 nm) intermediate in high ionic strength conditions (100 mM KP_i buffer) over a range of pH 5 – 7 (**Figure 2**). Because these measurements were carried out under high ionic strength where the dissociation rates of the complex out compete the oxidation reactions, we expect the kinetics to reflect weighted averages of the reactivities provided by the heterogeneous F-Glu variants. Indeed, in all cases the initial oxidation rates are mono-phasic (**Figure 2 and Table S3)**. Y191 and Y191 F-E_G CcP showed virtually the same low Cc oxidation activity and no pH dependence, indicating that F-E at non-232 sites had minimal effect on reactivity. Conversely, for Y191:E232 and Y191:F-E232 F-E_G CcP, the ferryl species grew in and decayed rapidly at low pH, commensurate with increased

rates of Cc oxidation relative to Y191 alone (**Table S3**). However, at higher pH (pH 7), Y191:E232 and Y191:F-E232 F-E_G exhibited slower Y191-like kinetics, with Y191:E232 retaining greater activity than the Y191:F-E232 F-E_G (**Figure 3a**).

Having established that global F-Glu incorporation does not greatly perturb CcP reactivity, we sought to better quantify the pH-dependent rate differences between Y191:E232 and Y191:F-E232 F-E_G by considering the 50:50 mixture of Y191:F-E232 and Y191:E232. If the ability of E232 to accelerate ET from Cc depends on a hydrogen bond to Y191, the lower pK_a of F-E232 may generate behavior similar to that of Y191:E232, but in a lower pH range. Modeling the rate

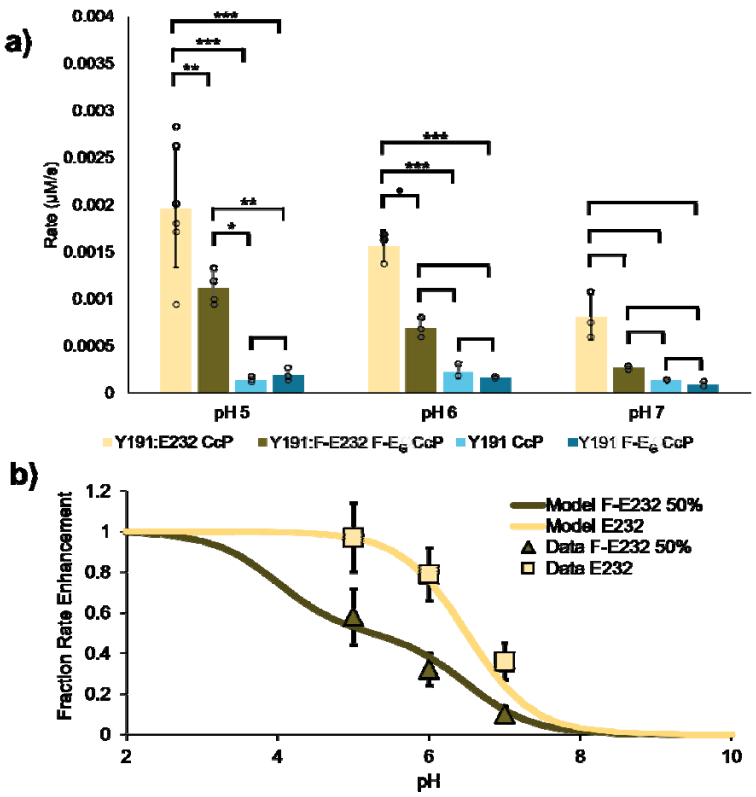

Figure 3. Initial rates of Cc oxidation by Y191 CcP variants. **a)** Y191 and Y191:F-E232 F-E_G CcP lack any pH dependency and CcP activity is mostly lost. Y191:F-E232 F-E_G was slower than Y191:E232 in all buffers regardless of pH and the Cc oxidation rate decreases to slower Y191-like kinetics at high pH for both variants. One-way ANOVA and post-hoc Tukey analysis was performed to evaluate statistical significance for each pH condition. Adjusted p-values are indicated where large statistical differences are observed (*** for $p < 0.001$, ** for $0.001 \leq p < 0.01$, and * for $0.01 \leq p < 0.05$). **b)** Comparison of a one and two proton ionization model to observed initial rates of Y191:E232 CcP and Y191:F-E232 F-E_G CcP, respectively. Y191:F-E232 F-E_G CcP rate assumes a 50:50 mixture of E232 and F-E232 in the sample.

enhancement by a one- and two- proton ionization model for Y191:E232 CcP and Y191:F-E232 F-E_G CcP, respectively, reasonably predicted the relative pH-dependency of each system. (**Figure 3b, Table S3**). The pH trends from the deprotonation of the E/F-E232-H^+-Y191$^\bullet$ triad

model the data reasonably well when a pK_a of 6.5 is assigned to E232 and 4.0 to F-E232 and a 50:50 mixture of the two components is assumed in the Y191:F-E232 F-E_G sample, as indicated by mass-spec. Thus, Y191:F-E232 F-E_G CcP is unable to stabilize a proton in the F-E232-H^+-Y191$^\bullet$ triad at elevated pHs (pH > 4) owing to its depressed pK_a, and that the associated loss of a hydrogen bond to Y191 lowers its potential such that ET from Cc Fe(II) is reduced.

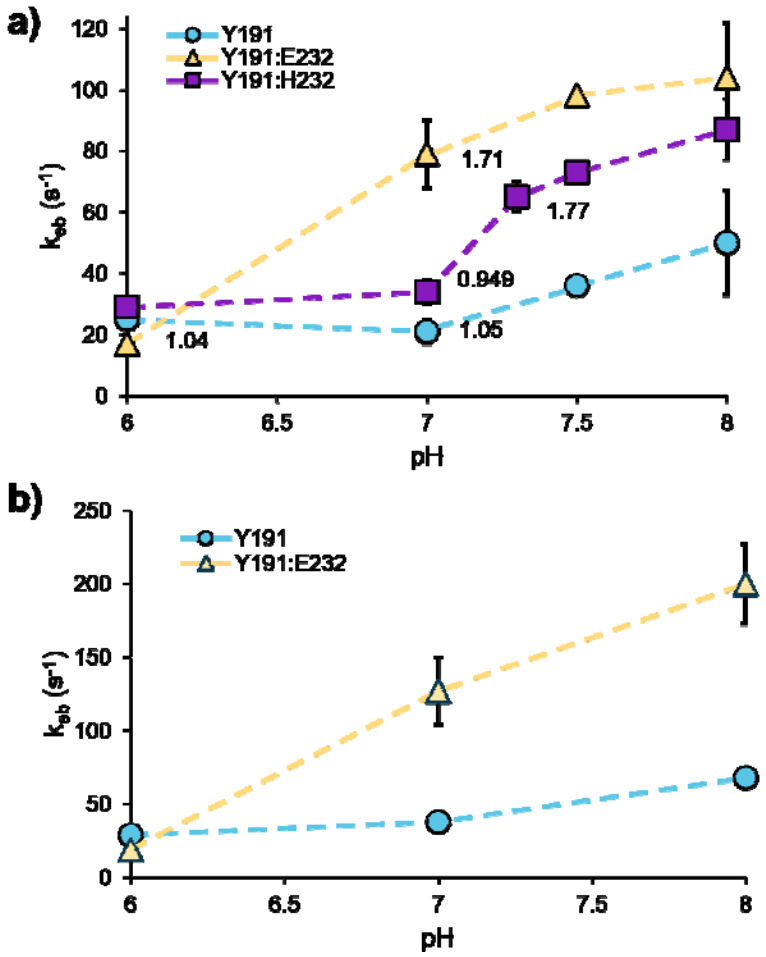

Figure 4. Back electron transfer rate constant (k_{eb}) as a function of pH for Y191 (blue), Y191:E232 (gold), and Y191:H232 (purple) CcP variants in complex with Cc in **a)** 100 mM Kpi Buffer and **b)** 10 mM Kpi Buffer. Kinetic solvent isotope effects (KSIE) are noted by corresponding data points when measured. k_{eb} has pH dependence for both the Y191:E232 and Y191:H232 variants and KSIEs track with increases in k_{eb}.

PCET facilitates Y191 oxidation in the ZnCcP variants

The ZnCcP:Cc redox photocycles were measured with time-resolved spectroscopy across pH 6-8 for the Y191-substituted variants. In low and high ionic strength buffers, the Y191:E232 and Y191:H232 ZnCcP variants exhibited much greater pH dependencies compared to Y191 alone (**Figure 4**). For Y191:E232, k_{eb} increases 4-fold between pH 6 and 7, whereas k_{eb} for Y191:H232 increases similarly at a higher pH of 7.3 (**Table S4**). This trend is different than what was observed previously for the FeCcP peroxide reaction, for which the rates of Cc oxidation decrease at higher pH in both the E232 and H232 variants. The decrease of reactivity at higher pH was assumed to derive from the H-bonded E/H232-H^+-Y191$^\bullet$ triad deprotonating and thereby depressing the reduction potential of Tyr$^\bullet$ [24]. For ZnCcP, the pH rate dependence also correlated with the relative pK_a values of the adjacent Glu and His residues, but in this case, rates enhanced in the higher pH ranges, thereby suggesting that Tyr deprotonation by the conjugate base during formation of Y191$^\bullet$ is critical for the photocycle (**Figure 4**). Both high and low ionic strength conditions generate similar pH trends for Y191 and Y191:E232 (**Figure 4**). The pHs where rates increase for E232 and H232 (7 and 7.5-8, respectively) shifted higher than the pK_as of the isolated residues (4.25 and 6.0 respectively), presumably owing to their protein environment, which includes proximity to $ZnP^{\bullet+}$. Consistent with a PCET mechanism, both the E232 and H232 variants showed a deuterium kinetic solvent isotope effect (KSIE), only at the pH values where rates increased. Y191:E232 gave a near 2-fold decrease in k_{eb} in the pD 7 deuterated buffer compared to the protonated pH 7 counterpart (**Table S5**). Similarly, Y191:H232 ZnCcP only exhibited a KSIE above pH 7.3, where k_{eb} also significantly increased. Notably, solvent deuterium substitution also modestly affects ionization properties (i.e. K_W and

pK_a values) with the neutral point being ~7.4 in D_2O. This shift could affect the pH range over which the conjugate base ionizes and thereby potentially contribute to an apparent KSIE. However, we only observed a KSIE in the pH range where there was already rate acceleration, i.e. the conjugate base had ionized to act as a proton acceptor and hence the KSIE likely reflects

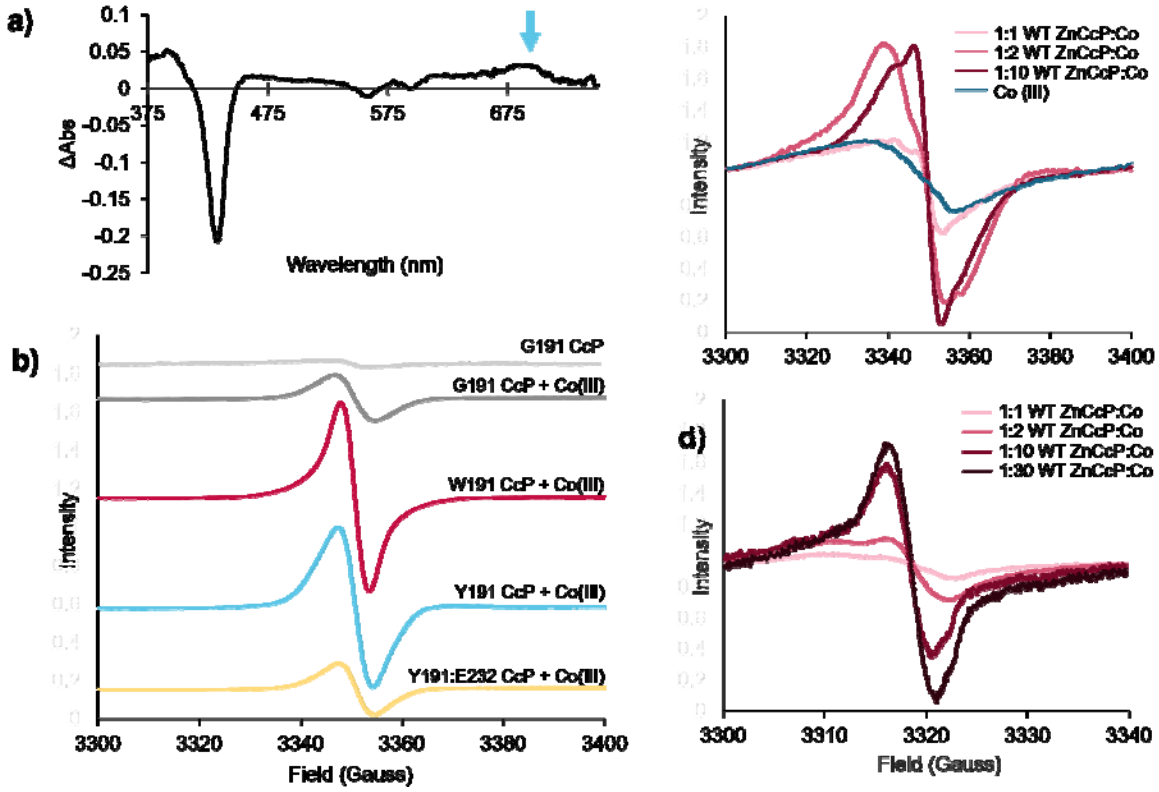

Figure 5. Characterization of of wt (red), G191 (dark gray), Y191 (blue), and Y191:E232 (gold) ZnCcP variants with CoN_5. **a)** TA difference spectra of Y191 ZnCcP reveal $ZnP^{\bullet+}$ species (indicated by a blue arrow) at 690 nm. **b)** cwEPR at 10 K, pH 6 of ZnCcP mutants with 10-fold excess of CoN_5 reveal organic radical formation present. In contrast, G191 CcP alone (light gray) has little to no signal in the spectra. The W191 containing wt CcP sample appears to have a slightly narrower signal than the other 191 variants indicative of a different radical species. cwEPR of wt ZnCcP at pH 6 with varying amounts of CoN_5 at **c)** 10 K and **d)** 110 K reveal splitting of two radical species. Shoulder peak likely correlates with $W191^{\bullet+}$.

the ability of the conjugate base to deprotonate Y191 in concert with oxidation by $ZnP^{\bullet+}$.

Radical distributions in photo-oxidized ZnCcP

The difference in formal potential between $ZnP^{\bullet+}$ and $W/Y191^{\bullet(+)}$ is a critical parameter in the ability of ZnCcP to oxidize Cc [32], but because the recombination reaction of $(ZnP/W191)^{\bullet+}$ with Cc Fe(II) is faster than the reduction of Cc Fe(III) by the ^3ZnP [33], $(ZnP/W191)^{\bullet+}$ is challenging to characterize. To address this issue, a sacrificial electron acceptor $[Co(NH_3)_5Cl]Cl_2$ (CoN_5) was used in place of Fe(III) Cc (**Scheme 2**). When reduced by ^3ZnP, CoN_5 decomposes into $Co(H_2O)_6^{2+}$, which diffuses and has a higher reduction potential than the precursor, and thus does not readily reduce $ZnP^{\bullet+}$. The transient absorption (TA) difference spectra of Y191 ZnCcP after photoexcitation with CoN_5 revealed a $ZnP^{\bullet+}$ species at 690 nm that was stable for at least 10 minutes (**Figure 5a**). X-band continuous wave electron paramagnetic resonance (cwEPR) spectroscopy confirmed the presence of an organic radical in W191 ZnCcP and Y191 ZnCcP, whereas the G191 substitution produced a similar but much lower amplitude cwEPR signal compared to W191 and Y191 (**Figure 5b**). Given the fast relaxation rate of $ZnP^{\bullet+}$ (T_1 = 1.5 – 16 ms) at 10 K compared to $W/Y191^{\bullet(+)}$ (T_1 > 35 ms), the $Trp^{\bullet+}/Tyr^{\bullet}$ transition saturates at 10 K and these spectra derive primarily from $ZnP^{\bullet+}$ (**Table S6**).

To better isolate the radical species contributing to the cwEPR spectra, the ratio between ZnCcP and CoN_5 was varied. Initially, ZnCcP samples were measured at 10 K with 10-fold excess CoN_5 to maximize yields of radical formation. Lowering the amount of CoN_5 to stoichiometric ratios decreased the dominant resonance attributed to $ZnP^{\bullet+}$ and revealed a previously obscured broad EPR signal (**Figure 5c**), likely derived from oxidation of W191 by $ZnP^{\bullet+}$. Unlike the sharper fast-relaxing signal from $ZnP^{\bullet+}$, the EPR transition of the likely

$W191^{\bullet+}$ relaxes slowly and saturates with the microwave power used at 10 K. At 110 K the saturation effect can be avoided by using a 40 dB attenuation (0.02 mW microwave power). The $W191^{\bullet+}$ signal is then more prominent and can be distinguished from the $ZnP^{\bullet+}$ signal (**Figure 5d**). Stoichiometric amounts of CoN_5 to ZnCcP gave rise to the highest relative signal of $W191^{\bullet+}$ compared to $ZnP^{\bullet+}$. Notably, no organic radicals directly form with light excitation of heme-containing CcP and CoN_5 (**Figure S2**), thereby indicating that oxidation of ZnP precedes radical formation at W191. For the G191 variant at low CoN_5 stoichiometry, cw-EPR, and measurements of T_m and T_1 at 60 K and 110 K indicated a high proportion of the fast-relaxing $ZnP^{\bullet+}$ (**Table S6**). The lack of substantial radical propagation in G191 ZnCcP, differs from the heme-peroxide reaction, wherein the G191 FeCcP:Cc primarily produces a peripheral $Tyr^{\bullet}$ radical upon reaction with peroxide [20]. This difference in reactivity between FeCcP and ZnCcP G191 suggests that the peroxide-derived Cpd I more readily oxidizes peripheral sites because it has a higher potential than $ZnP^{\bullet+}$. In all cases, there was no dipolar line broadening of the $ZnP^{\bullet+}$ signal, which appeared the same among the variants, including G191. The lack of broadening suggests that $ZnP^{\bullet+}$ and $W191^{\bullet+}$ bi-radicals (which would be separated by 7-8 Å) do not contribute appreciably to these spectra. When the CoN_5 ratio is low, $ZnP^{\bullet+}$ reacts to form $W191^{\bullet+}$, whose redox potential is comparable, but lower than that of $ZnP^{\bullet+}$; hence we observe a mixture of $ZnP^{\bullet+}$ and $W191^{\bullet+}$ in the sample. As shown below, DFT calculations performed over an MD trajectory indicate that the radical likely exchanges between the two sites. Given that the $ZnP^{\bullet+}$ and $W191^{\bullet+}$ resonances differ by ~1-14 G ($\Delta\nu$ ~ 3-14 MHz); k_f^{ex}, the ET rate corresponding to:

$$ZnP^{\bullet+}\,W191 \underset{k_b^{ex}}{\overset{k_f^{ex}}{\rightleftharpoons}} ZnP\,W191^{\bullet+}$$

must be considerably less than this value, i.e. $1x10^6 – 1x10^7$ s^{-1}, which is on the same order as the rate constant for the single step ET reaction from step 4 in **Scheme 1**, k_{eb} ($2x10^6$ s^{-1}) [36]. In contrast, when the CoN_5 ratio is high, additional reaction of photoexcited ZnP produced more of the porphyrin radical, which dominated the spectrum (**Scheme 3**).

Scheme 3. Reaction scheme for biradical production in ZnCcP

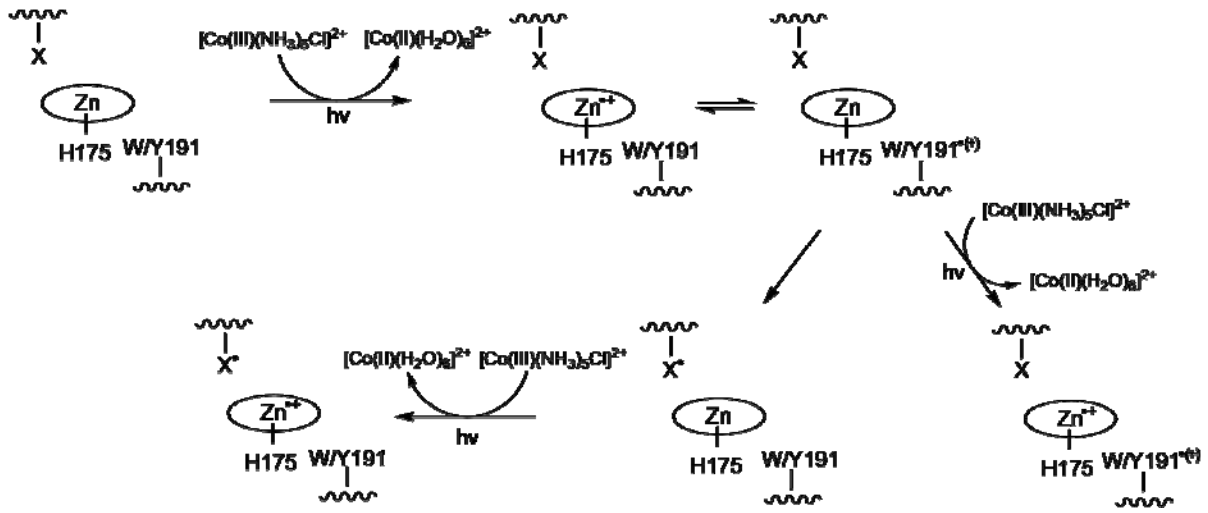

Photoreduction of the Y191-substituted CcP variants with CoN_5 at stoichiometric ratios were studied by cwEPR by in situ steady-state irradiation at room temperature. This approach produced cwEPR signals characteristic of $ZnP^{\bullet+}$ with a smaller contribution from a broad shoulder near the $ZnP^{\bullet+}$ peak, which may be from tyrosyl or another organic radical in the sample ($X^{\bullet}$, **Figure 6b-d**). Furthermore, the spectra were pH dependent, with the $ZnP^{\bullet+}$ signal dissipating at higher pH, but the broader, low-field signal persisting. The pH dependence also varied among the Y191 variants, with loss of the $ZnP^{\bullet+}$ signal at pH 8 for the Y191 variant, pH 7 for Y191:E232 and pH 6 for Y191:H232 (**Figure 6, Table S7**). These results may relate to the ET kinetics of the ZnCcP:Cc complex, where higher pH values (7-8), increase the ET rate from Cc owing to greater yield of radical character at the relay site. For Y191:E232, higher pH

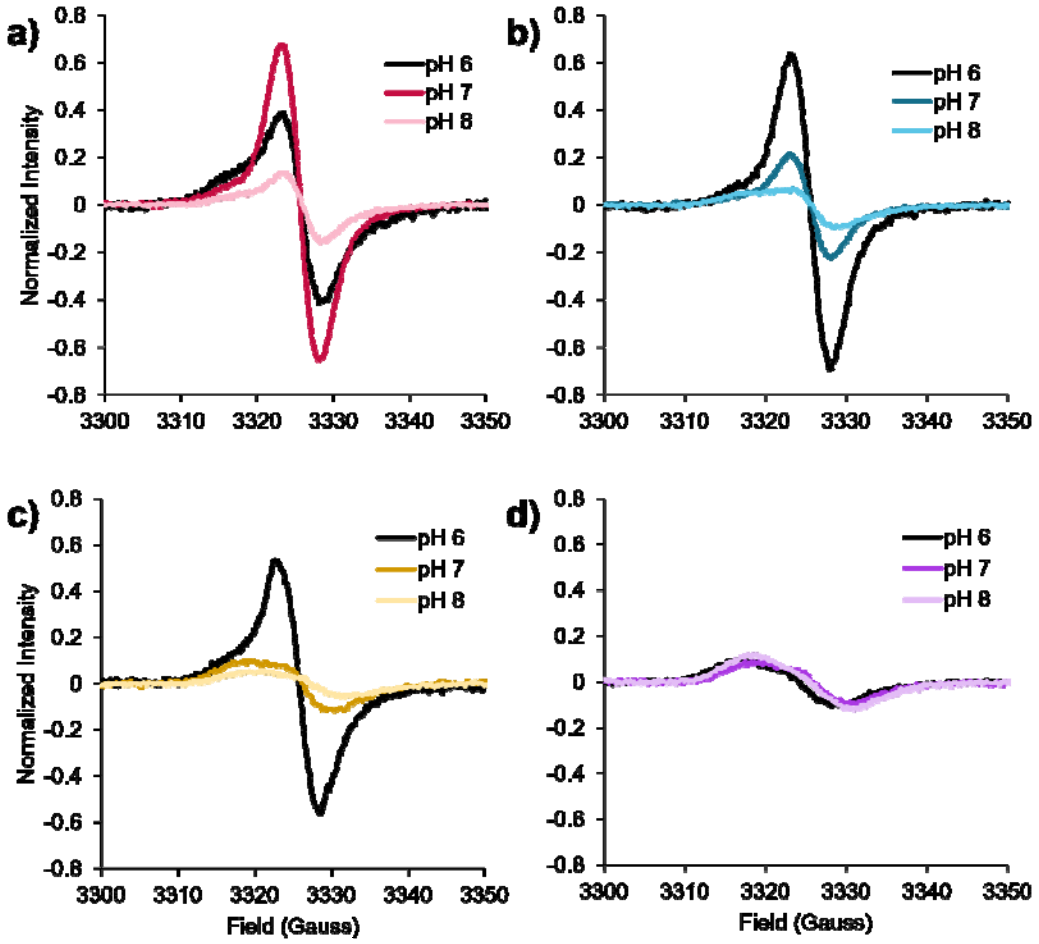

Figure 6. cwEPR spectra recorded at 293 K of **a)** W191, **b)** Y191, **c)** Y191:E232, and **d)** Y191:H232 variants with one-molar equivalent of CoN_5. Y191 and Y191:E232 ZnCcP variants exhibit pH-dependent behaviors of their cw spectra that track similarly as their ET rates in **Figure 3** where $X^{\bullet}$ is more prevalent in high pH conditions. Y191:H232 ZnCcP differs from the others in that the low-field radical is the only species present at all pH conditions.

deprotonates E232, which then accepts a proton from Y191 to form the tyrosyl radical; for the

Y191 without a conjugate base, yet higher pH is required for solvent to likely assist in Y191

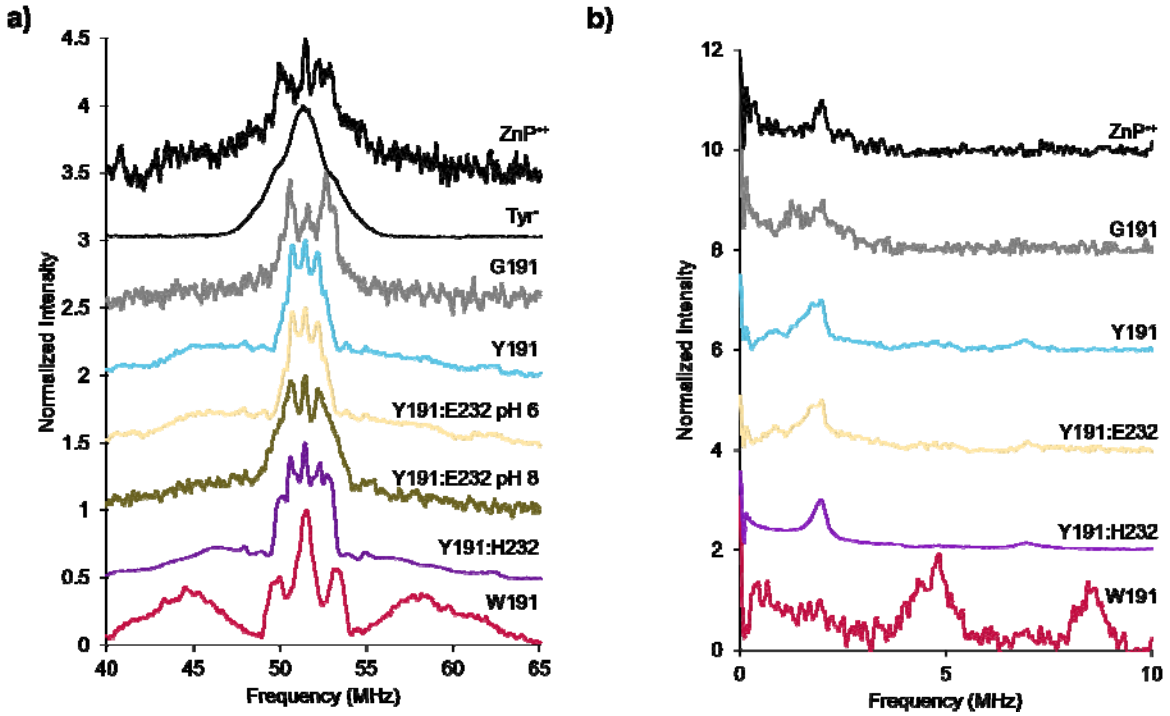

Figure 7. Hyperfine spectroscopy of ZnCcP radical species. **a)** ^{1}H ENDOR spectra of free ZnP$^{\bullet+}$and Tyr$^{\bullet}$ and of ZnCcP variants at 110 K, pH 6 (and pH 8 for Y191:E232) with equimolar CoN_5. The EPR observation frequency at 34 GHz was chosen to emphasize proton coupling to the low-field organic radical. Central peaks representing the proton Larmor frequency are present in spectra of all ZnCcP species. Signals from hyperfine-shifted Trp$^{\bullet+}$ protons are also present in W191 ZnCcP at 15 MHz whereas Y191 variants contain a broad peak at 8 MHz. G191 also exhibits some shoulder, but signal-to-noise is low. Tyr$^{\bullet}$ signal is shown for comparison. See **Figure S3** for simulation of the W191 spectrum. **b)** ^{14}N ESEEM spectra at 60 K, pH 6 also centered on the low-field radical transition of free ZnP$^{\bullet+}$ and ZnCcP variants with equimolar CoN_5. A sharp peak at 2 MHz is attributed to ^{14}N-coupling in the porphyrin. Spectra of the W191 and Y191 variants both include additional peaks at 5 and 7-8 MHz, due to hyperfine interactions with indole nitrogen in Trp. Y191 samples likely propagate the radical to nearby Trp residues. See **Figures S4-S5** for simulations.

deprotonation; for Y191:H232 the EPR spectra surprisingly showed no pH dependence with the broad, low-field peak present at pHs 6-8 and little indication of ZnP$^{\bullet+}$. One might expect H232 to

deprotonate at even higher pH than E232, but the higher H232 pK_a may also favor the interaction of the neutral imidazole with the Y191 hydroxyl and thereby poise the Y191 proton for transfer.

Pulsed EPR techniques were carried out to further characterize the radical species generated in each ZnCcP variant by CoN_5 quenching. ^{1}H Davies electron nuclear double resonance (ENDOR) spectra of W191 ZnCcP at high CoN_5 stoichiometry (10:1) and low temperature 10 K, revealed hyperfine coupling interactions characteristic of free $ZnP^{\bullet+}$ in solution (**Figure S2a**). There are also broad hyperfine interactions at ~15 MHz that resemble those of $W191^{\bullet+}$ from CcP Cpd I [18]. To better isolate the hyperfine interactions of the non-$ZnP^{+\bullet}$ radical, $X^{\bullet}$, ^{1}H Davies ENDOR was carried out at low CoN_5, 110 K, pH 6, with the ENDOR resonance centered on the low field peak (**Figure 7a**). The $ZnP^{\bullet+}$ control showed few hyperfine interactions at this field, but the W191 ZnCcP gave broad, considerably shifted peaks, characteristic of $W191^{\bullet+}$, which are consistent with simulated data from published parameters for the $W191^{\bullet+}$ species of CcP Cpd I [37] (**Figure S3**). Note that in Cpd I, $W191^{\bullet+}$ is weakly coupled to the S=1 ferryl heme, which is not the case here [18,21,22]. Y191 and Y191:E232 produced similar ENDOR spectra to each other under these conditions, but that of Y191:H232 contains additional shoulder peaks indicative of $X^{\bullet}$ (**Figure 7a**). At pH 8, the Y191:E232 spectrum resembles more closely the Y191:H232 spectrum, as it also contains shoulder peaks. The G191 ENDOR spectrum also contains some peaks similar to $ZnP^{\bullet+}$, but no broad shoulders (**Figure 7a**).

^{14}N electron spin echo envelope modulation (ESEEM) spectroscopy was utilized to further characterize $X^{\bullet}$ (**Figure 7b**). Resonances in free $ZnP^{\bullet+}$ and G191 ZnCcP at 2 MHz arise from the coupling of the ZnP radical to nitrogen in the porphyrin pyrrole rings. This feature is also observed in the Y191 ZnCcP variants where $ZnP^{\bullet+}$ is still present in appreciable amounts. In addition to this interaction, both the W191 and Y191 variants also exhibit a pair of peaks with

resonances located around 5 MHz and 7-8 MHz. With these coupling intensities and frequencies, it seems unlikely that $X^{\bullet}$ derives from only a tyrosyl radical, which usually has no nitrogen hyperfine coupling [38–40] or very weak (<1 MHz) nitrogen couplings from residues in the vicinity of the tyrosyl radical [41]. This nitrogen coupling indicates that a migrated tryptophanyl radical is at least partially responsible for these signals (**Figure 7b**). The positions of ESEEM signals were generally insensitive to temperature but accentuated at 60 K compared to 110 K (**Figures S2**). Simulation of the W191 ESEEM-derived hyperfine parameters (**Figure S4**) matched reasonably well with the ENDOR results and those calculated previously [37]. For the Y191 variant ESEEM spectra, only the ~2 MHz peak could be accurately simulated; the resulting hyperfine parameters do not match those calculated previously for neutral or cationic Trp radicals in CcP, and argue in favor of some other species than Trp, i.e. ZnP (**Figure S5**). Thus, with CoN_5 replacing Cc and preventing recombination, the primary $ZnP^{\bullet+}$ radical partially migrated through $Y191^{\bullet}$ to peripheral Trp residues in the protein. Radical migration depended on 1) first forming $Y191^{\bullet}$, which is facilitated by Y191 deprotonation and 2) maintaining a suitably high $Y191^{\bullet}$ potential to oxidize peripheral sites, which is facilitated by hydrogen bonding from the deprotonating residue. Thus, proton environment modulates Y191 reactivity in several ways, producing different pH dependencies for different variants: the Y191 variant activates the relay site to migrate the radical at pH 8, Y191:E232 does so at pH 7 or higher, and Y191:H232 does so at pH 6 or higher.

QM/MM -MD calculations

QM/MM structure optimizations followed by spin density analysis along QM/MM MD trajectories revealed distinct radical localization patterns in the W191 and Y191 ZnCcP variants (**Figure 8**). In $(ZnP/W191)^{\bullet+}$, alternating radical character between $ZnP^{\bullet+}$ and $Trp^{\bullet+}$ was observed

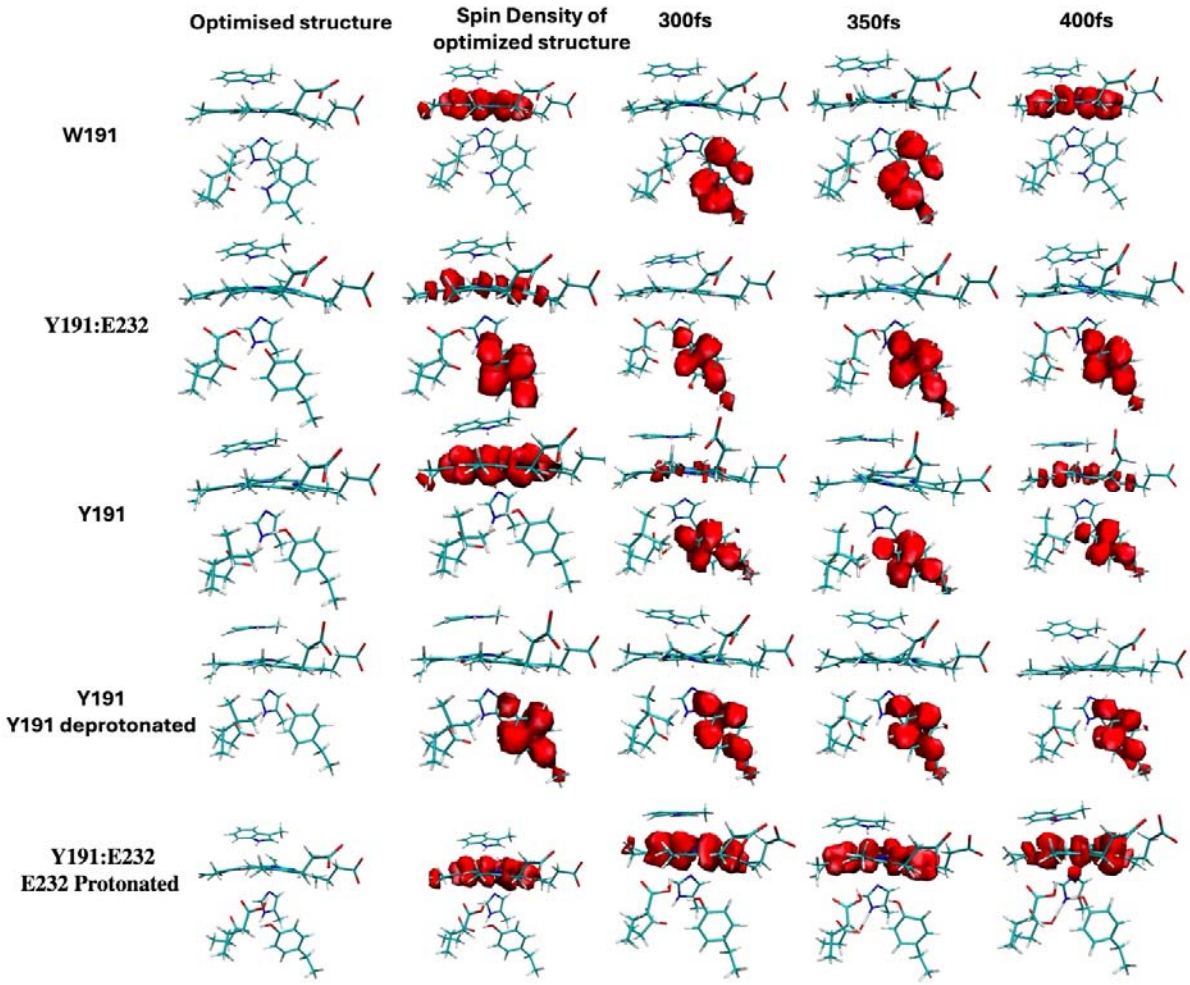

Figure 8. Spin density obtained from DFT with the wB97x functional as a function of time along the QM/MM MD trajectory for the different variants characterized experimentally. Three snapshots drawn from a 1ps long trajectory (additional structures in SI Figures S6-S10) highlight the key differences in behavior of the three variants and the importance of PCET in enabling hole transfer between ZnP and W191/Y191. E232 deprotonation facilitates proton transfer and radical formation at

over the MD trajectory, consistent with EPR features for both radicals when the CoN_5 stoichiometry was low. The calculations suggest that K_{eq} lies toward $Trp^{\bullet+}$, with the $Trp^{\bullet+}/ZnP^{+}$ ratio ~ 1.8, which agrees with the distribution found by EPR spectroscopy, averaged over the pH range of measurements (**Table S7**, **Figure S8**). It is interesting that the QM/MM simulations here yield different results from previous work [33,37], which found greater delocalization of the hole over $(ZnP/Trp)^{\bullet+}$ and hole occupancy favoring $ZnP^{\bullet+}$. We consider two possible reasons for the discrepancy. First, whereas both studies use DFT to calculate spin density in the QM region, the wB97x functional employed here is a range-separated hybrid that proves more accurate for spin densities than B3LYP (additional discussion in the SI). Second, because the prior work focused on the larger question of identifying the residues that participate in the long-range ET process [33], whereas the present study is focused on the question of hole localization and the effect of proton transfer on the relay residue, the former applied longer, but less accurate MD trajectories, whereas the latter applied shorter, but more accurate QM/MM MD trajectories.

For Y191:E232 with E232 deprotonated, the simulations indicated nearly immediate proton transfer from Y191 to E232 accompanied by radical localization on $Y191^{\bullet}$ (**Figure 8**, Row 2), thereby supporting a possible PCET mechanism that is consistent with the experimentally observed solvent isotope effects. When Y191:E232 was modeled with protonated (neutral) E232, spin density localized exclusively on $ZnP^{\bullet+}$, (**Figure 8**, Row 5) underscoring the role of proton transfer in facilitating $Tyr^{\bullet}$ formation and corroborating the pH-dependent rate studies. For the Y191 variant, $(ZnP/Y191)^{\bullet(+)}$, QM/MM trajectories suggest the Y191 proton transfers instead to D235 and spin density again predominantly localizes on Tyr. However, in the experimental system, proton transfer to D235 is unlikely to occur as ET rates remain low with only D235 in vicinity of Y191. Interestingly, in the simulations, partial $ZnP^{\bullet+}$ radical character

appears when a hydrogen bond formed between D235 and Y191$^{\bullet}$ in the MD trajectory, reflecting the ability of a hydrogen bond to increase the reduction potential of Y191$^{\bullet}$.

Discussion

The W191$^{\bullet+}$ hole-hopping site is both necessary for long-range ET in the CcP:Cc system and also sensitive to perturbation. Only when supplemented with specific surrounding interactions can Tyr substitute for Trp in this capacity. Oxidizable Tyr residues also serve as relay sites in other protein systems such as PSII, but due in part to the large differences in pK_a between tryptophanyl and tyrosyl radicals, they are not functionally interchangeable with Trp [42]. In FeCcP:Cc, substitution of W191 for Tyr eliminates ET activity, but can be rescued by the introduction of an adjacent conjugate base from either His or Glu. The decreases in oxidation rates of Cc(II) by Cpd I in the CcP Y191:E/H232 variants with increasing pH [24] derive from deprotonation of the E/H232-H^+-Y191$^{\bullet}$ triad and the subsequent lowering of the Y191$^{\bullet}$ reduction potential. The loss of rate enhancement at lower pHs by substitution of E232 with 4-fluoro-glutamic acid further supports this mechanism. Y191:F-E232 behaves like Y191:E232 CcP, but with a lower pK_a (**Figure 3**). Based on the predicted pK_a of F-Glu, we would expect the Y191:F-E232 F-E_G CcP, Cc(II) oxidation rates to increase further at lower pHs (3-4); however, due to protein instability, the reaction could not be measured at these low pHs. Because F-E232 is a better proton donor than E232, at pHs where F-E232 remains protonated the hydrogen bond donated to Y191$^{\bullet}$ may be more effective at increasing the Y191$^{\bullet}$ redox potential than with E232. However, it was challenging to measure ET at these low pHs and combined with the complications of partial F-E232 incorporation, this issue remains unresolved. Nonetheless, the isosteric substitution of F-E232 strongly supports the ability of a nearby proton to tune the

potential of Y191$^{\bullet}$ into a range where it can act as an effective ET relay site for peroxide-driven oxidation of Cc (II).

Rate enhancement in the peroxide-activated FeCcP:Cc system shows an opposite pH trend compared to the photo-activated ZnCcP:Cc system, with larger solvent pH decreasing k_{eb} in the former and increasing k_{eb} in the latter (**Figure 4, Table S4**). For FeCcP, a hydrogen bond to Y191$^{\bullet}$ from E/H232 provides a high-enough reduction potential to oxidize Cc; as pH increases, this potential-elevating proton is lost. However, for ZnCcP, the preceding oxidation of Y191 by ZnP$^{\bullet+}$ is likely the pH-sensitive reaction. ZnP$^{\bullet+}$ - mediated oxidation of Y191 is facilitated by PCET from Y191 to E/H232 (or solvent) and at lower pHs, a protonated conjugate base (or lack of a solvent hydroxide ion) prevents transfer of the Y191 proton. A similar effect is observed in PSII where the oxidations of both Tyr_D and Tyr_Z are coupled to proton transfers to hydrogen-bonded His residues; when the His residues are protonated at low pH, the Tyr residues are nonfunctional as relay sites. Moreover, function of Tyr_Z could be restored by solvent or high pH when the hydrogen-bonded base was removed, indicative of Tyr_Z deprotonation to solvent upon oxidation [10-12]. Such an interpretation also implies that Cpd I in the peroxide CcP reaction has a higher reduction potential relative to Y191 than ZnP$^{\bullet+}$ in the photochemical system because with FeCcP, the pH sensitive reaction involves the latter step, i.e. oxidation of Fe(II) Cc by the already formed Y191$^{\bullet}$. Notably, even if the lower relative reduction potential of ZnP$^{\bullet+}$ compared to Cpd I requires initial Y191$^{\bullet}$ activation by PCET, a subsequent hydrogen bond back from the conjugate base to Y191$^{\bullet}$ may still facilitate the oxidation of Cc Fe(II), and radical propagation with a sacrificial electron acceptor.

For ZnCcP, the pH range where rate enhancement manifests is somewhat higher than that predicted by the pK_a of free Glu. However, it is not uncommon for the pK_a of residues within the

protein interior to be perturbed 5-6 pH values higher than their solution pK_as with Glu residues having pK_a increases from 4 to around 7 [43,44]. Studies of pH-dependent reactivity for F-E232 ZnCcP were not pursued because ZnCcP exhibited a perturbed UV/Vis spectrum after ZnP incorporation, suggesting that the reconstituted system was structurally perturbed in some manner.

The difference in reduction potential between $ZnP^{\bullet+}$ and $W/Y191^{\bullet(+)}$ is a critical parameter in determining the efficacy of an ET relay site. Past computational studies have estimated $K_{eq} < 1$ [32–34], which is required to weight the otherwise large rate constant for ET between Fe(II)Cc and $Trp^{\bullet+}$ (> 10^8 sec^{-1}) [34]. Use of CoN_5 as an oxidative quencher to photoexcited $ZnP^{\bullet+}$ stabilized the protein radical against recombination with the external reductant. No radical species formed when FeCcP underwent the same irradiation protocol (**Figure S2a**). $ZnP^{\bullet+}$ reacts further to form $W191^{\bullet+}$ and the cation radical distributes between the two sites, favoring $Trp^{\bullet+}$. Both the experimental fits to the EPR data averaged across the pHs and the QM/MM trajectories give a similar ~1.8:1 ratio of $Trp^{\bullet+}/ZnP^{\bullet+}$ after ZnCcP oxidation, hence placing the $Trp^{\bullet+}$ radical ~

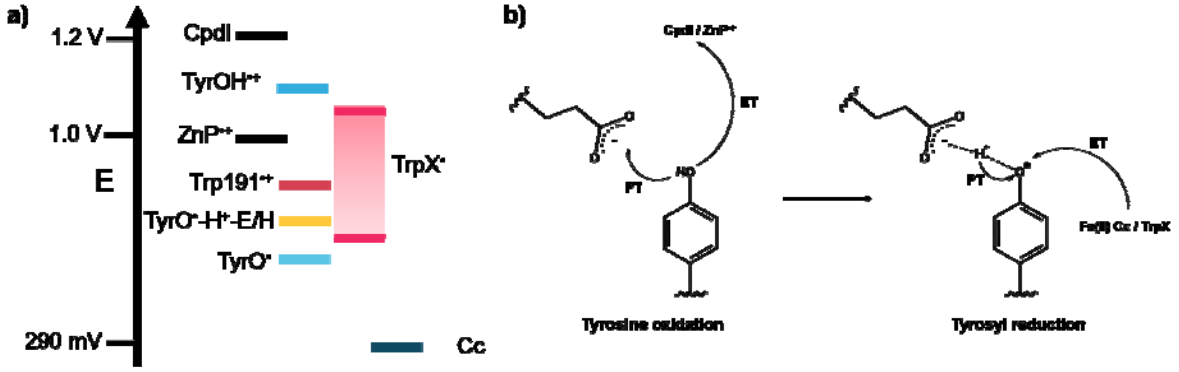

Figure 9. a) Proposed potential energy diagram for oxidizable species in CcP:Cc. **b)** PCET steps in Cc oxidation by CcP. In ZnCcP, the oxidation of Y191 becomes rate limiting because the $TyrOH^{\bullet+}$ potential is too high relative to that of $ZnP^{\bullet+}$ for the Tyr to be oxidized in the absence of PCET.

15 mV in formal potential below that of $ZnP^{\bullet+}$, which is 1.0 - 1.1 V [33] (**Figure 9a**). With k_{obs} ~ 10^6 sec^{-1} and K_{eq} > 1; the ET rate between $ZnP^{\bullet+}$ and W191 must be considerably slower than expected. Indeed, the lack of line broadening in the EPR experiments suggests that the exchange rate is <10^7 s^{-1}. At higher stoichiometries of the oxidative quencher, some ZnP is available for reoxidation potentially creating a second radical on $ZnP^{\bullet+}$. Pulsed-dipolar EPR spectroscopy provided some evidence for bi-radicals in these systems, but the yields were low and the signals difficult to interpret.

For similar experiments with the Y191 ZnCcP and CoN_5, a low-field broadened peak also appears in the EPR spectrum along with the characteristic $ZnP^{\bullet+}$ signal; and its population depends differently on pH among the 232 variants. ESEEM suggests ^{14}N hyperfine coupling to this transition, and thus some contribution from a tryptophanyl radical is most likely (**Figure 7b**). For Y191:H232, the low-field peak is dominant at pH 6-8, with little contribution from $ZnP^{\bullet+}$, for Y191:E232, this is the case for pH 7 and above, and for Y191 alone, the low field peak begins to dominate at pH 8. This same trend is also observed in the ^1H ENDOR of the low field transition (**Figure 7a**). In all three cases, the spectral transition is associated with loss of $ZnP^{\bullet+}$, presumably because of its ability to oxidize the 191 position. Consistent with the ZnCcP:Cc oxidation experiments, a hydrogen bond acceptor (E/H232) close to Y191, facilitates PCET from Y191 to $ZnP^{\bullet+}$, but the pH range where Y191 activates, depends on the 232 conjugate base. Y191:H232 propagates the radical most effectively at low pH, where the H232 should remain protonated and unable to assist in Y191 deprotonation. However, we suspect that given the close proximity of H232 to Y191, its imidazole moiety remains neutral and hydrogen bonds to the Y191 hydroxyl, even at low pH. After Y191 oxidizes, and the hydroxyl proton transfer to the base, the radical at least partially migrates from $Y191^{\bullet}$ to a peripheral Trp residue, as evidenced by its low-field,

broad resonance and ^{14}N hyperfine interactions. A hydrogen bond from the conjugate base back to Y191$^{\bullet}$ may increase the Y191$^{\bullet}$ potential sufficiently to oxidize these peripheral sites. The ENDOR spectra of Y191:E232 resembles that of Y191 at pH 6, but at pH 8, additional hyperfine shoulder peaks arise in Y191:E232, much like those seen for Y191:H232. Thus, although ZnP$^{\bullet+}$ can oxidize Y191 to some extent in all cases, the radical primarily propagates to the peripheral sites when there is a conjugate base present to hydrogen bond with Y191$^{\bullet}$. Given these are long-time scale experiments, the peripheral site is likely a thermodynamic sink, but one that can only be accessed when the relay residue is appropriately tuned to oxidize it.

Regardless of the identity of the migrated radical in the Y191 variants, ZnP$^{\bullet+}$ does not oxidize Y191 as easily as the W191 residue unless oxidation couples to Y191 deprotonation, either by elevated pH or a neighboring base. In contrast, Cpd I in FeCcP can oxidize the 191 site regardless of pH [23,24]. Thus, the formal potential of ZnP$^{\bullet+}$ must be lower than that of Cpd I (**Figure 9a**). Considering that there are two ET steps involved in Cc(II) oxidation by ZnP$^{\bullet+}$, the observed PCET effects could arise from the oxidation of Y191 by ZnP$^{\bullet+}$ and/or the reduction of Y191$^{\bullet}$ by Cc (**Figure 9b**). Both the peroxide dependent reaction [24] and the ZnCcP photochemical oxidation of Cc show a modest KSIE under conditions where the relay site is activated and rates are enhanced. PCET reactions can either proceed through step-wise or concerted mechanisms and have been shown to switch between these mechanisms depending on pH [42,45–48]. In the case of the Y191 FeCcP:Cc complex, potential vs proton-affinity dependencies suggest that the proton-coupled reaction likely proceeds with rate-limiting Y191 oxidation followed by sequential proton transfer (PT) [24]. However, in the ZnCcP system rates are only enhanced and radicals propagate to peripheral sites under conditions where a base aids the oxidation of the 191 relay site – a situation more likely to be governed by a concerted

electron-proton transfer (CEPT) mechanism or sequential mechanism where the PT is rate limiting (**Figure 4**) [47,49]. Cationic Tyr radicals in proteins are extremely short lived (~ 1 ps) and have low pKa values of ~ -2 [50,51], thus once oxidized, PT from $Y191^{\bullet+}$ is unlikely to be rate limiting [52]. Finally, our experimental data and computational modeling indicate that ET between $ZnP^{\bullet+}$ and W191 is slower than originally thought, with neither fast exchange nor hole delocalization between the two sites. Despite their relatively close proximity, ZnP and W191 are not effectively coupled, presumably owing to the relative orientations of the participating orbitals. Thus, it's interesting to consider that protein conformation may be capable of altering donor-acceptor orientation in a manner that substantially modulates multi-step ET reactions.

Conclusions

Overall, our results demonstrate the detailed roles that PCET and hydrogen bonds play in modulating the reactivity of a hole-hopping relay site in a protein. Introduction of a proton acceptor for a tyrosyl radical rescues ET from Cc and alters radical propagation within ZnCcP. The proton acceptor has different functions depending on the relative potentials of the photogenerated acceptor ($ZnP^{\bullet+}$) and the ultimate donor (Cc or a peripheral protein site). The interacting conjugate base facilitates Tyr oxidation through PCET, and tunes the resulting radical reduction potential through hydrogen bonding. In the case of peroxide-generated CpdI, which has high reactivity, Y191 oxidizes readily, but requires the hydrogen bond to retain a high enough potential to oxidize the donor site. In the case of the lower potential $ZnP^{\bullet+}$, the proton acceptor assists in deprotonation of the Tyr residue, effectively lowering its potential and thereby activating the relay site. An ensuing hydrogen bond to the oxidized $Tyr^{\bullet}$ again raises its potential to migrate the radical from the reaction center. These results also imply a reduction potential

scale in the CcP system wherein CpdI > $Y191^{\bullet}$ ~ $ZnP^{\bullet+}$ > $W191^{\bullet+}$. For both FeCcP and ZnCcP, the high yield of $W191^{\bullet+}$ localizes the hole closer to the biological donor Cc Fe(II), and is the primary electron acceptor on Cc. This work has implications for how proteins control the propagation of high-potential radical centers through hydrogen-bonding perturbations to relay sites, which, in principle, could be brought under allosteric regulation.

Materials & Methods

Protein expression and purification

CcP was expressed and purified as described previously [23,24]. *Escherichia coli* BL21(DE3) cells were transformed with the CcP gene in a ppSUMO vector and grown at 37°C in LB with 50 μg/mL kanamycin. When the $OD_{600\ nm}$ reached between 0.7 and 0.9, cells were induced with 100 μM isopropyl β-D-1-thiogalactopyranoside (IPTG) and expressed at 20 °C overnight. Cells were lysed via sonication, and soluble protein was isolated by centrifugation. CcP was purified from lysate using a Ni-NTA column and His-SUMO tags were cleaved with ULP-1(R3) protease. Tags were removed on a Ni-NTA column and CcP was collected in the flow through. For Fe-CcP, the protein was stirred overnight at 4 °C with 1 molar equivalent of hemin dissolved in 0.1 M NaOH. The reaction was then neutralized with acetic acid and centrifuged to remove precipitated heme. For ZnCcP, the protein was stirred for 1 – 5 days at 4 °C with 2 – 5 molar excess of Zn protoporphyrin IX dissolved in DMF. Both FeCcP and ZnCcP were further purified via size exclusion chromatography and anion exchange chromatography. Fractions with $A_{408nm}/A_{280nm} \geq 1$ for FeCcP and $A_{432nm}/A_{280nm} \geq 2$ for ZnCcP were collected and concentrated. Proteins were then flash frozen in liquid nitrogen, and stored at -80 °C.

Cc was expressed in BL21(DE3) cells containing the cytochrome c maturation system. Cell cultures were grown at at 37 °C in LB with 125 μg/mL ampicillin and 50 μg/mL δ-aminolevulenic acid, a precursor for heme production. The PBTR-1 vector with the Cc gene contains a *trc* and autoinduces Cc expression during the growth. Cells were lysed via sonication and Cc was purified out of the lysate via cation exchange chromatography and size exclusion chromatography. Protein was concentrated, flash frozen, and stored at -80 ° C.

Global incorporation of 4-fluoro-glutamic acid

A tac promotor was cloned into the ppSUMO vector containing the CcP gene using primers tacF and tacR (**Table S2**). Overlap extension PCR cloning was performed and PCR products were digested with DpnI to remove the ppSUMO template. DNA sequences were confirmed via Sanger sequencing. F-CcP variants were expressed in *E. coli* PA340 cells from the Coli Genetic Stock Center collection which are auxotrophic for glutamic acid. Cells were grown at 37 °C in LB with 50 μg/mL kanamycin. When the OD_{600} reached ~0.8 cells were spun down and washed with Nanopure water several times before resuspending in M9 minimal media with 50 μg/mL kanamycin and 100 μg/mL 4-fluoro-DL-glutamic acid. The cells were then induced with 100 μM isopropyl β-D-1-thiogalactopyranoside (IPTG) and expressed at 17 °C overnight. The F-Glu containing proteins were purified as described above, and the presence of F-Glu residues were confirmed via mass spectrometry.

Multiple Turnover Reduction Kinetics

Cc was reduced with dithionite and buffer exchanged into a 100 mM KP_i buffer at the appropriate pH. Multiple turnover measurements were conducted with 1800 μL of 100 μM CcP

and 30 μM reduced Cc in 100 mM KP_i buffer (pH 5 – 7) at 10 °C. An excess of Cc (Fe^{2+}) was used to minimize binding effects from Cc (Fe^{3+}). Reactions were initiated by the rapid addition H_2O_2 while stirring at 700 RPM (Hewlett-Packard 89090A Peltier) with a final H_2O_2 concentration of 10 μM. The rate of Cc (Fe^{2+}) oxidation was monitored at the heme Q bands $Abs_{550\ nm}$ - $Abs_{540\ nm}$ (ε = 19.2 $mM^{-1}\ cm^{-1}$) and, the CcP oxy-ferryl species at $Abs_{434\ nm}$ (a Cc (Fe^{2+}/Fe^{3+}) isosbestic point) using a Hewlett-Packard Agilent 8453 spectrophotometer. Given that peroxide was in excess and reaction between peroxide and CcP fast, at early times the reaction was considered under pseudo first-order conditions. Rate constants were obtained by fitting the Cc oxidation traces to monoexponential curves (MatLab; Mathworks):

$$y = a * e^{-b*x} + c$$

Transient Absorption Spectroscopy (TA)

To avoid triplet state quenching from ground state oxygen, ZnCcP samples were prepared anaerobically. Cc was oxidized by potassium ferricyanide and was buffer exchanged into a degassed 10 or 100 mM KP_i buffer (pH/D 6 – 8). Samples were prepared in a 1 mm cuvette with a 4 μL drop containing 75 μM ZnCcP and 75 – 150 μM Cc (Fe^{3+}). ZnCcP alone was also measured for each variant to determine the rate of triplet state decay to the ground state (k_D). Transient absorption measurements were performed as described previously [13]. Samples were placed in the path of a probe light, provided by a 75 W Xe-arc lamp and were excited at 560 nm by an Opotek Opolette Nd:YAG laser with approximately 2 mJ of power per 8 ns pulse firing at 20 Hz. The time delays between the excitation pump source and probe light were controlled by a Digital Delay Generator DG355 (Stanford Research Systems) which was triggered by the laser Q-switch. Time delays were varied between 0 to 40 ms randomly to reduce effects of

photobleaching. Absorption from the probe light was measured using a Hamamatsu Photonic Multichannel Analyzer (PMA) and averaged 50 times. Difference spectra were calculated as ΔA = -log(excited/reference). Data were subjected to global analysis and singular value decomposition (SVD) was used to deconvolute the evolution-associated difference spectra (EADS) in Glotoran [53].

Electron Paramagnetic Resonance Spectroscopy

Samples for Electron Paramagnetic Resonance (EPR) spectroscopy were prepared anaerobically in 100 mM KP_i (pH 6 – 8) and 20 % glycerol buffer. A $[Co(NH_3)_5Cl]\ Cl_2$ stock solution was prepared and degassed to act as a sacrificial electron acceptor for ^{3}ZnP. 150 – 750 µM CcP was added to 150 – 1,500 µM $[Co(NH_3)_5Cl]\ Cl_2$ for molar ratios ranging from 1:1 to 1:30. Around 20µL of the sample were inserted in Quartz capillary (Wilmad WG-221T-RB) with an internal diameter of 1.1 mm. The capillary were sealed with epoxy in a Coy Lab's anaerobic chamber. Samples were either excited at 560 nm and flash-frozen or kept at room temperature and excited during collection for low and high temperature studies, respectively.

cw-EPR spectra were conducted using a Bruker E500 ElexSys spectrometer equipped with a ER 4123SHQE Bruker cavity. For 10 K measurements, the spectrometer was equipped with a liquid He cryostat. The acquisition parameters were fixed to 40 dB (0.02 mW) microwave power, 5G modulation amplitude and 100 kHz modulation frequency. For 110 K measurements, the temperature was stabilized by flushing cold Nitrogen air through a transfer line to the cavity. The acquisition parameters were fixed to 40 dB (0.02 mW) microwave power, 5 G modulation amplitude and 100 kHz modulation frequency. For 298 K measurements, the acquisition parameters were 15 dB (6.35 mW) microwave power, 20 dB receiver gain, 4 G modulation

amplitude and 100 kHz modulation frequency. In situ irradiation was achieved with a 5 mW diode laser at $\lambda = 532 \pm 10$ nm.

Pulse EPR experiments were conducted at 34 GHz using an Elexsys E580 spectrometer equipped with a 10 W solid state amplifier. All experiments were achieved in a Q-Band ENDOR EN 5107D2 Cavity. A Bruker E-580 AWG Arbitrary Waveform Generator was used for the microwave pulse generation. The temperature was varied by using an ER 4118HV-CF10-L FlexLine Cryogen-Free VT System. The pulse length (varying with the coupling range of the resonator and the microwave power used) was determined with a rabi nutation measurement π-τ2-π/2-τ-π-τ-echo by increasing sequentially the length of the first pulse.

The electron spin–lattice relaxation times T_1 were measured over the temperature range by varying the repetition rate (or shot repetition time SRT) in two pulse echo sequence, π/2-τ- π-τ-echo. The magnetization recovery was fitted by systematically a mono (single radical species) and bi-exponential (double radical species) model. T_1 value are reported in the **Table S6**. Phase-memory times T_m were measured by a two-pulse echo decay sequence, π/2-τ-π-τ-echo, while varying the tau. The curves were fit by an exponential decay: $I(t)=I_0*\exp(-2t/T_m)$ or biexponential decay $I(t)=I_1*\exp(-2\tau/T_{m1}) + I_2*\exp(-2\tau/T_{m2})$.

ENDOR (Electron Nuclear Double Resonance) measurements were conducted with a ^{1}H Davies sequence π-t_1-rf pulse-t_2-π/2-t-π-t-echo as the hfccs of some protons can be very large for the tryptophanyl radical by instance (~20 MHz for some positions). t_1 and t_2 were fixed to 1 µs to avoid the overlap of the rf pulse with microwave pulses. The rf pulse length has been fixed to 20 µs, length that shows the maximum proton NMR resonance intensity with the 150 W Bruker RF amplifier used. Selective π/2 and π pulses were used with a length around 70/140 ns respectively in accordance with a microwave power attenuation of 15 dB.

3-pulse ESEEM sequence π/2-τ-π/2-T-π/2-τ-echo was employed in Q-band to study the spin modulation of nitrogen couplings. To avoid any τ artifact, 12 slices of ESEEM was recorded with τ varying by steps of 10 ns and averaged during post-processing of the data. For every τ value, the 3P-ESEEM was recorded using a starting mixing time T = 100 ns and a dwell time of 8 ns to have sufficient frequency resolution in the area of 1-20 MHz. For this pulse experiment, the resonator was critically coupled and a length of 14 ns was employed for π/2 pulses.

Fitting of the cw-EPR spectra were carried out by the easyspin toolbox under Matlab. The garlic.m function was employed to fit spectrum with 2 components. The first component with large linewidth was simulated with the use of four parameters: a fixed single ^{1}H hyperfine coupling constant of 17 MHz (6.06 G), and three variables parameters: isotropic gfactor g_1, a gaussian linewidth (broadening peak to peak) lw_1, and a scaling factor A_1 [54]. The second component with narrower linewidth was simulated with the use of three variables parameters: an isotropic gfactor g_2, a gaussian linewidth (broadening peak to peak) lw_2, and a scaling factor A_2. The sum of the scaling factor was fixed to unity: $A_1 + A_2 = 1$.

ESEEM and ENDOR spectra were simulated using saffron.m function of the easyspin matlab toolbox.

QM/MM Calculations and Analysis

The PDB file 1u74, 6p41, 5cih is used as the initial structure (provided in the github folder) for the W191, Y191:E232, and Y191 variants of ZnCcP:Cc. respectively. The protein forcefield is taken from CHARMM22 [55] and H molecules are added according to the topology file. The protein is solvated in a rectangular box of TIP3P water molecules. The size of the box is determined by the length of the protein; a 20 □ layer of water molecules is added around the

protein (**Figure S6a-b**) and a 0.05M buffer is added to make the system charge neutral. The solvent is then equilibrated with a 200-step steepest decent (SD) algorithm and a 1000-step Adopted Basis Newton-Raphson (ABNR) simulation. The structure obtained after MD equilibration are optimized at the QM/MM level using the software package Py-ChemShell [56], where QM calculations are performed with ORCA and the MD simulations use DL-POLY5.

Following previous experimental work and theoretical studies on the 2-step mechanism in the ZnCcP:Cc [23,34], we undertake QM/MM simulations to elucidate hole hopping between the ZnP and the W191/Y191 residues. The QM active site includes the porphyrin ring, axial histidine (HIS) residue (resid 175), Asp (resid 235), Trp/Tyr (resid 191), Leu/Glu (resid 232), and Trp (resid 51) as shown in **Figure S6c**. Initial QM/MM optimization with MM region frozen and using basis: 6-31G* with functionals B3LYP, WB97x and electrostatic embedding [57]. We find that the range-separated wB97x hybrid functional yields more accurate orbital energies and spin densities for the triplet and doublet states and choose this functional for the remaining calculations (**Figure S7** and accompanying text in the SI). We generate a 1ps long QM/MM-MD (NVT) trajectory for the W191, Y191, Y191:E232 variants with structures saved every 50 fs. Spin density analysis is performed using these snapshots to track hole localization (**Figures S8-S10**). To validate the pH-dependence studies, we run shorter (500 ps) trajectories for the protonated Y191:E232 and the deprotonated Y191 variants (**Figures S11-S12**).

Supporting Information

The following files are available free of charge.

Additional details including DNA sequences and primers used for mutagenesis. Tables of fitted kinetic data for multiple-turnover and TA experiments. Tables for radical relaxation times and

distributions in EPR measurements. XIC for MS of F-Glu containing peptides. Additional EPR data including controls. Optimized MD structures, along with additional simulation details, motivation for choice of DFT functional, and QM/MM trajectory spin-density plots for all variants discussed in the manuscript. A GitHub Repository link is also provided where all relevant structure files, input files, and results of spin density analysis are included. (DOC)

Author Information

Corresponding Author:

*Brian R Crane, Department of Chemistry and Chemical Biology, Weill Institute for Cell and Molecular Biology, National Biomedical Center for Advanced ESR Technologies (ACERT), Cornell University, Email: bc69@cornell.edu, Phone: 607-254-8634

Authors:

Rebecca K Zawistowski, Department of Chemistry and Chemical Biology, Weill Institute for Cell and Molecular Biology, Cornell University, Email: rkz8@cornell.edu

Timothée Chauviré, Department of Chemistry and Chemical Biology, Weill Institute for Cell and Molecular Biology, National Biomedical Center for Advanced ESR Technologies (ACERT), Cornell University, Email: tsc84@cornell.edu, ORCID ID: 0000-0002-9466-4785

Sutanuka Manna, Department of Chemistry and Chemical Biology, Cornell University, Email: sm2837@cornell.edu

Nandini Ananth, Department of Chemistry and Chemical Biology, Cornell University, Email: ananth@cornell.edu

Acknowledgements

This work is supported by NSF grant MCB 2129729 to BRC and by ACERT under the NIH grant 1R24GM146107 and the NIH grant 1R35GM158400-01 to NA. We would like to thank Siddarth Chandrasekaran for the initial EPR measurements and analysis as well as Estella Yee for assistance with kinetics measurements.

References

[1] J.L. Dempsey, J.R. Winkler, H.B. Gray, Proton-Coupled Electron Flow in Protein Redox Machines, Chem. Rev. 110 (2010) 7024–7039. https://doi.org/10.1021/cr100182b.

[2] N. Nelson, C.F. Yocum, Structure and function of photosystems I and II, Annu. Rev. Plant Biol. 57 (2006) 521–565. https://doi.org/10.1146/annurev.arplant.57.032905.105350.

[3] V.R.I. Kaila, M.I. Verkhovsky, M. Wikström, Proton-coupled electron transfer in cytochrome oxidase, Chem. Rev. 110 (2010) 7062–7081. https://doi.org/10.1021/cr1002003.

[4] J.J. Warren, M.E. Ener, A. Vlček, J.R. Winkler, H.B. Gray, Electron hopping through proteins, Coord. Chem. Rev. 256 (2012) 2478–2487. https://doi.org/10.1016/j.ccr.2012.03.032.

[5] C. Shih, A.K. Museth, M. Abrahamsson, A.M. Blanco-Rodriguez, A.J. Di Bilio, J. Sudhamsu, B.R. Crane, K.L. Ronayne, M. Towrie, A. Vlček, J.H. Richards, J.R. Winkler, H.B. Gray, Tryptophan-accelerated electron flow through proteins, Science (80-.). 320 (2008) 1760–1762. https://doi.org/10.1126/science.1158241.

[6] J.A. Stubbe, Protein Radical Involvement in Biological Catalysis?, Annu. Rev. Bioc 58 (1989) 257–285.

[7] D.E. Westmoreland, P.R. Feliciano, G. Kang, C. Cui, A. Kim, J. Stubbe, D.G. Nocera, C.L. Drennan, 2.6-Å resolution cryo-EM structure of a class Ia ribonucleotide reductase trapped with mechanism-based inhibitor N3CDP, Proc. Natl. Acad. Sci. 121 (2024). https://doi.org/10.1073/pnas.

[8] J.T.M. Kennis, T. Mathes, Molecular eyes: Proteins that transform light into biological information, Interface Focus 3 (2013). https://doi.org/10.1098/rsfs.2013.0005.

[9] B.A. Barry, Proton coupled electron transfer and redox active tyrosines in Photosystem II, J. Photochem. Photobiol. B Biol. 104 (2011) 60–71. https://doi.org/10.1016/j.jphotobiol.2011.01.026.

[10] L. Hammarstrom, S. Styring, Proton-coupled electron transfer of tyrosines in Photosystem II and model systems for artificial photosynthesis: the role of a redox-active link between catalyst and photosensitizer, Energy Enviornmental Sci. 4 (2011) 2379–2388. https://doi.org/10.1039/c1ee01348c.

[11] S. Styring, J. Sjöholm, F. Mamedov, Two tyrosines that changed the world: Interfacing the oxidizing power of photochemistry to water splitting in photosystem II, Biochim. Biophys. Acta - Bioenerg. 1817 (2012) 76–87. https://doi.org/10.1016/j.bbabio.2011.03.016.

[12] F. Mamedov, R.T. Sayre, S. Styring, Involvement of histidine 190 on the D1 protein in electron/proton transfer reactions on the donor side of photosystem II, Biochemistry 37 (1998) 14245–14256. https://doi.org/10.1021/bi980194j.

[13] L. Gerhards, A. Deser, D.R. Kattnig, J. Matysik, I.A. Solov'yov, Weak Radiofrequency Field Effects on Biological Systems Mediated through the Radical Pair Mechanism, Chem. Rev. 125 (2025) 8051–8088. https://doi.org/10.1021/acs.chemrev.5c00178.

[14] J. Xu, L.E. Jarocha, T. Zollitsch, M. Konowalczyk, K.B. Henbest, S. Richert, M.J. Golesworthy, J. Schmidt, V. Déjean, D.J.C. Sowood, M. Bassetto, J. Luo, J.R. Walton, J. Fleming, Y. Wei, T.L. Pitcher, G. Moise, M. Herrmann, H. Yin, H. Wu, R. Bartölke, S.J.

Käsehagen, S. Horst, G. Dautaj, P.D.F. Murton, A.S. Gehrckens, Y. Chelliah, J.S. Takahashi, K.W. Koch, S. Weber, I.A. Solov'yov, C. Xie, S.R. Mackenzie, C.R. Timmel, H. Mouritsen, P.J. Hore, Magnetic sensitivity of cryptochrome 4 from a migratory songbird, Nature 594 (2021) 535–540. https://doi.org/10.1038/s41586-021-03618-9.

[15] J.M. Nocek, J.S. Zhou, S. De Forest, S. Priyadarshy, D.N. Beratan, J.N. Onuchic, B.M. Huffman, Theory and practice of electron transfer within protein-protein complexes: Application to the multidomain binding of cytochrome c by cytochrome c peroxidase, Chem. Rev. 96 (1996) 2459–2489. https://doi.org/10.1021/cr9500444.

[16] J.E. Erman, L.B. Vitello, J.M. Mauro, J. Kraut, Detection of an Oxyferryl Porphyrin π-Cation-Radical Intermediate in the Reaction between Hydrogen Peroxide and a Mutant Yeast Cytochrome c Peroxidase. Evidence for Tryptophan-191 Involvement in the Radical Site of Compound, Biochemistry 28 (1989) 7992–7995. https://doi.org/10.1021/bi00446a004.

[17] J.E. Huyett, P.E. Doan, R. Gurbiel, A.L.P. Houseman, M. Sivaraja, B.M. Hoffman, D.B. Goodir, Compound ES of Cytochrome c Peroxidase Contains a Trp π-Cation Radical: Characterization by CW and Pulsed Q-Band ENDOR Spectroscopy, J. Am. Chem. Soc. 117 (1995) 9033–9041. https://doi.org/10.1021/ja00140a021.

[18] M. Sivaraja, D.B. Goodin, M. Smith, B.M. Hoffman, Identification by ENDOR of Trp191 as the Free-Radical Site in Cytochrome c Peroxidase Compound ES, Science (80-.). 245 (1989) 738–740.

[19] M.A. Miller, A complete mechanism for steady-state oxidation of yeast cytochrome c by yeast cytochrome c peroxidase, Biochemistry 35 (1996) 15791–15799. https://doi.org/10.1021/bi961488c.

[20] A. Ivancich, P. Dorlet, D.B. Goodin, S. Un, R. V October, V. Re, M. Recei, V. March, Multifrequency High-Field EPR Study of the Tryptophanyl and Tyrosyl Radical Intermediates in Wild-Type and the W191G Mutant of Cytochrome c Peroxidase, (2001) 6107–6115. https://doi.org/10.1021/ja0036514.

[21] A.L.P. Houseman, P.E. Doan, D.B. Goodin, B.M. Hoffman, Comprehensive Explanation of the Anomalous EPR Spectra of Wild-Type and Mutant Cytochrome c Peroxidase Compound ES, Biochemistry 32 (1993) 4430–4443. https://doi.org/10.1021/bi00067a036.

[22] B.M. Hoffman, J.E. Roberts, C.H. Kang, E. Margoliash, Electron paramagnetic and electron nuclear double resonance of the hydrogen peroxide compound of cytochrome c peroxidase., J. Biol. Chem. 256 (1981) 6556–6564. https://doi.org/10.1016/s0021-9258(19)69025-3.

[23] T.M. Payne, E.F. Yee, B. Dzikovski, B.R. Crane, Constraints on the Radical Cation Center of Cytochrome c Peroxidase for Electron Transfer from Cytochrome c, Biochemistry 55 (2016) 4807–4822. https://doi.org/10.1021/acs.biochem.6b00262.

[24] E.F. Yee, B. Dzikovski, B.R. Crane, Tuning Radical Relay Residues by Proton Management Rescues Protein Electron Hopping, J. Am. Chem. Soc. 141 (2019) 17571–17587. https://doi.org/10.1021/jacs.9b05715.

[25] Q. Zhu, A. V. Soudackov, C. Tommos, S. Hammes-Schiffer, Proton-Coupled Electron Transfer upon Oxidation of Tyrosine in a De Novo Protein: Analysis of Proton Acceptor Candidates, Biochemistry 63 (2024) 1999–2008. https://doi.org/10.1021/acs.biochem.4c00211.

[26] J.M. Nocek, E.D.A. Stemp, M.G. Finnegan, T.I. Koshy, M.K. Johnson, E. Margoliash, A. Grant Mauk, M. Smith, B.M. Hoffman, Low-Temperature, Cooperative Conformational Transition within [Zn-Cytochrome C Peroxidase, Cytochrome c] Complexes: Variation with Cytochrome, J. Am. Chem. Soc. 113 (1991) 6822–6831. https://doi.org/10.1021/ja00018a017.

[27] S.A. Wallin, E.D.A. Stemp, A.M. Everest, J.M. Nocek, B.M. Hoffman, T.L. Netzel, Multiphasic Intracomplex Electron Transfer from Cytochrome c to Zn Cytochrome c Peroxidase: Conformational Control of Reactivity, J. Am. Chem. Soc. 113 (1991) 1842–1844. https://doi.org/10.1021/ja00005a065.

[28] N. Liang, C.H. Kang, P.S. Ho, E. Margoliash, B.M. Hoffman, Long-Range Electron Transfer from Iron(II)-Cytochrome c to (Zinc-Cytochrome c Peroxidase)(+) within the 1:1 Complex, J. Am. Chem. Soc. 108 (1986) 4665–4666. https://doi.org/10.1021/ja00275a076.

[29] P.S. Ho, B.M. Hoffman, N. Solomon, C.H. Kang, E. Margoliash, Kinetics and Energetics of Intramolecular Electron Transfer in Yeast Cytochrome c Peroxidase, Biochemistry 23 (1984) 4122–4128. https://doi.org/10.1021/bi00313a017.

[30] E.D.A. Stemp, B.M. Hoffman, Cytochrome Peroxidase Binds Two Molecules of Cytochrome c: Evidence for a Low-Affinity, Electron-Transfer-Active Site on Cytochrome c Peroxidase, Biochemistry 32 (1993) 10848–10865. https://doi.org/10.1021/bi00091a041.

[31] S.A. Kang, P.J. Marjavaara, B.R. Crane, Electron transfer between cytochrome c and cytochome c peroxidase in single crystals, J. Am. Chem. Soc. 126 (2004) 10836–10837. https://doi.org/10.1021/ja049230u.

[32] X. Ru, B.R. Crane, P. Zhang, D.N. Beratan, Why Do Most Aromatics Fail to Support Hole Hopping in the Cytochrome c Peroxidase-Cytochrome c Complex?, J. Phys. Chem. B 125 (2021) 7763–7773. https://doi.org/10.1021/acs.jpcb.1c05064.

[33] N. Jiang, A. Kuznetsov, J.M. Nocek, B.M. Hoffman, B.R. Crane, X. Hu, D.N. Beratan, Distance-independent charge recombination kinetics in cytochrome c-cytochrome c peroxidase complexes: Compensating changes in the electronic coupling and reorganization energies, J. Phys. Chem. B 117 (2013) 9129–9141. https://doi.org/10.1021/jp401551t.

[34] F.H. Wallrapp, A.A. Voityuk, V. Guallar, In-silico Assessment of Protein-Protein Electron Transfer. A Case Study: Cytochrome c Peroxidase - Cytochrome c, PLoS Comput. Biol. 9 (2013) 1–7. https://doi.org/10.1371/journal.pcbi.1002990.

[35] E. Yamamoto, Y. Ishihama, N. Asakawa, Application of partially fluorinated carboxylic acids as ion-pairing reagents in LC/ESI-MS, Talanta 127 (2014) 219–224. https://doi.org/10.1016/j.talanta.2014.03.060.

[36] K. Wang, H. Mei, L. Geren, M.A. Miller, A. Saunders, X. Wang, J.L. Waldner, G.J. Pielak, B. Durham, F. Millett, Design of a ruthenium-cytochrome c derivative to measure electron transfer to the radical cation and oxyferryl heme in cytochrome c peroxidase, Biochemistry 35 (1996) 15107–15119. https://doi.org/10.1021/bi9611117.

[37] C. Bernini, E. Arezzini, R. Basosi, A. Sinicropi, In silico spectroscopy of tryptophan and tyrosine radicals involved in the long-range electron transfer of cytochrome c peroxidase, J. Phys. Chem. B 118 (2014) 9525–9537. https://doi.org/10.1021/jp5025153.

[38] J. McCracken, I.R. Vassiliev, E.C. Yang, K. Range, B.A. Barry, ESEEM studies of peptide nitrogen hyperfine coupling in tyrosyl radicals and model peptides, J. Phys. Chem. B 111 (2007) 6586–6592. https://doi.org/10.1021/jp071402x.

[39] A. Boussac, J.M. Verbavatz, M. Sugiura, Isotopic labelling of photosystem II in Thermosynechococcus elongatus, Photosynth. Res. 98 (2008) 285–292. https://doi.org/10.1007/s11120-008-9305-2.

[40] K. Warncke, G.T. Babcock, J. McCracken, Structure of the Y_D Tyrosine Radical in Photosystem II as Revealed by 2H Electron Spin Echo Envelope Modulation (ESEEM) Spectroscopic Analysis of Hydrogen Hyperfine Interactions, J. Am. Chem. Soc. 116 (1994) 7332–7340. https://doi.org/10.1021/ja00095a042.

[41] K.A. Campbell, J.M. Peloquin, B.A. Diner, X. Tang, D.A. Chisholm, R.D. Britt, The τ -Nitrogen of D2 Histidine 189 is the Hydrogen Bond Donor to the Tyrosine Radical $Y_D^{\bullet}$ of Photosystem II, 7863 (1997) 4787–4788.

[42] A. Migliore, N.F. Polizzi, M.J. Therien, D.N. Beratan, Biochemistry and Theory of Proton-Coupled Electron Transfer, Chem. Rev. 114 (2014) 3381–3465. https://doi.org/10.1021/cr4006654.

[43] M.J. Harms, J.L. Schlessman, G.R. Sue, E. Bertrand García-Moreno, Arginine residues at internal positions in a protein are always charged, Proc. Natl. Acad. Sci. U. S. A. 108 (2011) 18954–18959. https://doi.org/10.1073/pnas.1104808108.

[44] M.J. Harms, C.A. Castañeda, J.L. Schlessman, G.R. Sue, D.G. Isom, B.R. Cannon, B. García-Moreno E., The pKa Values of Acidic and Basic Residues Buried at the Same Internal

Location in a Protein Are Governed by Different Factors, J. Mol. Biol. 389 (2009) 34–47. https://doi.org/10.1016/j.jmb.2009.03.039.

[45] S.Y. Reece, D.G. Nocera, Proton-Coupled Electron Transfer in Biology: Results from Synergistic Studies in Natural and Model Systems, Annu. Rev. Biochem. 78 (2009) 673–699. https://doi.org/10.1146/annurev.biochem.78.080207.092132.

[46] S. Hammes-Schiffer, A.A. Stuchebrukhov, Theory of coupled electron and proton transfer reactions, Chem. Rev. 110 (2010) 6939–6960. https://doi.org/10.1021/cr1001436.

[47] I.J. Rhile, T.F. Markle, H. Nagao, A.G. Dipasquale, O.P. Lam, M. a Lockwood, K. Rotter, J.M. Mayer, Concerted Proton - Electron Transfer in the Oxidation of Hydrogen-Bonded Phenols, J. Am. Chem. Soc. 128 (2006) 6075–6088.

[48] A. Nilsen-Moe, C.R. Reinhardt, P. Huang, H. Agarwala, R. Lopes, M. Lasagna, S. Glover, S. Hammes-Schiffer, C. Tommos, L. Hammarström, Switching the proton-coupled electron transfer mechanism for non-canonical tyrosine residues in a de novo protein, Chem. Sci. 15 (2024) 3957–3970. https://doi.org/10.1039/d3sc05450k.

[49] M. Zhang, T. Irebo, O. Johansson, L. Hammarstrom, Proton-Coupled Electron Transfer from Tyrosine□: A Strong Rate Dependence on Intramolecular Proton Transfer Distance, J. Am. Chem. Soc. 133 (2011) 13224–13227. https://doi.org/10.1021/ja203483j.

[50] K. Pirisi, L. Nag, Z. Fekete, J.N. Iuliano, J. Tolentino Collado, I.P. Clark, I. Pécsi, P. Sournia, U. Liebl, G.M. Greetham, P.J. Tonge, S.R. Meech, M.H. Vos, A. Lukacs, Identification of the vibrational marker of tyrosine cation radical using ultrafast transient infrared spectroscopy

of flavoprotein systems, Photochem. Photobiol. Sci. 20 (2021) 369–378. https://doi.org/10.1007/s43630-021-00024-y.

[51] L. Nag, P. Sournia, H. Myllykallio, U. Liebl, M.H. Vos, Identification of the TyrOH•+ Radical Cation in the Flavoenzyme TrmFO, J. Am. Chem. Soc. 139 (2017) 11500–11505. https://doi.org/10.1021/jacs.7b04586.

[52] A. Harriman, Further comments on the redox potentials of tryptophan and tyrosine, J. Phys. Chem. 91 (1987) 6102–6104. https://doi.org/10.1021/j100308a011.

[53] J.J. Snellenburg, S.P. Laptenok, R. Seger, K.M. Mullen, I.H.M. van Stokkum, Glotaran□: A Java-Based Graphical User Interface for the R Package TIMP, J. Stat. Softw. 49 (2012).

[54] S. Stoll, A. Schweiger, EasySpin, a comprehensive software package for spectral simulation and analysis in EPR, J. Magn. Reson. 178 (2006) 42–55. https://doi.org/10.1016/j.jmr.2005.08.013.

[55] A.D. MacKerell, D. Bashford, M. Bellott, R.L. Dunbrack, J.D. Evanseck, M.J. Field, S. Fischer, J. Gao, H. Guo, S. Ha, D. Joseph-McCarthy, L. Kuchnir, K. Kuczera, F.T.K. Lau, C. Mattos, S. Michnick, T. Ngo, D.T. Nguyen, B. Prodhom, W.E. Reiher, B. Roux, M. Schlenkrich, J.C. Smith, R. Stote, J. Straub, M. Watanabe, J. Wiórkiewicz-Kuczera, D. Yin, M. Karplus, All-atom empirical potential for molecular modeling and dynamics studies of proteins, J. Phys. Chem. B 102 (1998) 3586–3616. https://doi.org/10.1021/jp973084f.

[56] S. Metz, J. Kästner, A.A. Sokol, T.W. Keal, P. Sherwood, ChemShell-a modular software package for QM/MM simulations, Wiley Interdiscip. Rev. Comput. Mol. Sci. 4 (2014) 101–110. https://doi.org/10.1002/wcms.1163.

[57] P. Sherwood, A.H. De Vries, M.F. Guest, G. Schreckenbach, C.R.A. Catlow, S.A. French, A.A. Sokol, S.T. Bromley, W. Thiel, A.J. Turner, S. Billeter, F. Terstegen, S. Thiel, J. Kendrick, S.C. Rogers, J. Casci, M. Watson, F. King, E. Karlsen, M. Sjøvoll, A. Fahmi, A. Schäfer, C. Lennartz, QUASI: A general purpose implementation of the QM/MM approach and its application to problems in catalysis, J. Mol. Struct. THEOCHEM 632 (2003) 1–28. https://doi.org/10.1016/s0166-1280(03)00285-9.

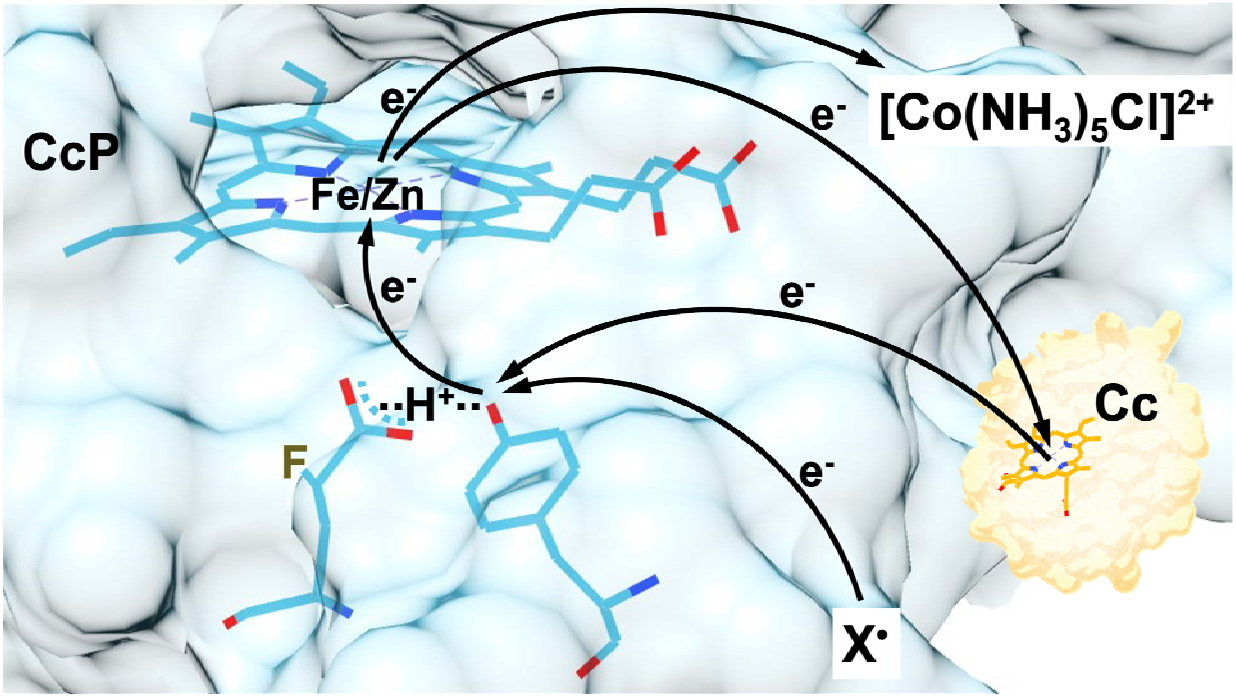
CcP
Fe/Zn
e-
e-
e-
e-
e-
[Co(NH3)5Cl]2+
Cc
..H+..
F
X•